A finite element approach combining a reduced-order system, Padé approximants, and an adaptive frequency windowing for fast multi-frequency solution of poro-acoustic problems

Romain Rumpler, Peter Göransson, Jean-François Deü

A finite element approach combining a reduced-order system, Padé approximants, and an adaptive frequency windowing for fast multi-frequency solution of poro-acoustic problems

R. Rumpler[1,2,*,†], P. Göransson[1] and J.-F. Deü[2]

[1]*The Marcus Wallenberg Laboratory for Sound and Vibration Research (MWL), Department of Aeronautical and Vehicle Engineering, School of Engineering Sciences, KTH Royal Institute of Technology, Stockholm SE-100 44, Sweden*
[2]*Structural Mechanics and Coupled Systems Laboratory (LMSSC), Conservatoire National des Arts et Métiers (CNAM), Paris 75003, France*

In this work, a solution strategy is investigated for the resolution of multi-frequency structural-acoustic problems including 3D modeling of poroelastic materials. The finite element method is used, together with a combination of a modal-based reduction of the poroelastic domain and a Padé-based reconstruction approach. It thus takes advantage of the reduced-size of the problem while further improving the computational efficiency by limiting the number of frequency resolutions of the full-sized problem. An adaptive procedure is proposed for the discretization of the frequency range into frequency intervals of reconstructed solution. The validation is presented on a 3D poro-acoustic example.

KEY WORDS: structural-acoustics; dissipative interface; noise reduction; reduced-order model; Padé approximants; poroelastic materials

1. INTRODUCTION

During the past two decades, computational methods have been increasing in importance as engineering tools in the effort of reducing noise for interior domains in vehicles. In the design process, several detailed structural-acoustic analyses need to be performed, and increasingly, the effects of interior trim components are included. However, modeling vibroacoustic problems with such dissipative interfaces as, for example, porous materials described with the Biot–Allard theory [1], can lead to prohibitive sizes of finite element (FE) models. It is therefore a question of considerable interest to propose efficient solution strategies.

Among the enhancements proposed in the past, use of equivalent acoustic impedances [2, 3] has proved to be very efficient but unfortunately limited by strong assumptions. In the scope of 3D FE modeling, the introduction of a mixed displacement-pressure porous formulation for the solid and fluid phases [4], respectively, downsized the number of DOFs per node from six, when using a standard solid and fluid phases displacement formulation [5, 6], to four DOFs. Hierarchical elements also proved to reduce the number of DOFs needed to model the porous media [7]. Recently, modal reduction techniques have been proposed and applied to standard linear poroelastic FEs, in

*Correspondence to: R. Rumpler, Department of Aeronautical and Vehicle Engineering, KTH Royal Institute of Technology, SE-100 44 Stockholm, Sweden.

†E-mail: rumpler@kth.se

an attempt to keep a fine and complex 3D modeling of the problem in the scope of low frequency applications [8–11].

Alternatively, in a more general approach, recent research has been carried out in order to propose reduced-order models targeting fast frequency sweeps for increasingly complex models. As such, Lanczos-based interpolatory methods, such as the Padé-via-Lanczos algorithm [12] or its subsequent development for more general partial fields and unsymmetric systems with the matrix-valued Padé-via-Lanczos approach [13–15], have been extended to second-order problems, being however limited to constant non-proportional damping models. Additionally, this extension is made by a linearization of the second-order problem, which involves doubling the dimension of the state-space vector, thus substantially increasing the memory requirements. To alleviate this drawback, second-order Arnoldi-based methods have been proposed [16], allowing for a structure-preserved reduced model, but still limited to constant non-proportional damping. It is only recently that a few methods have been developed for reduced-order models able to effectively account for general non-linear frequency-dependence of the linear system of equations [17–23], as is the case for refined modeling of sound absorbing porous materials. They are based on the explicit calculation of the solution vector and its derivatives at a restricted number of main frequencies in the spectrum of interest. In [20], these explicit derivatives are used to span a subspace, suitable for a reduced frequency interval in the spectrum, on which the global matrices are projected. The frequency sweep is then performed for a small system of linear equations. A drawback of this approach is that the possibly frequency-dependent global matrices may need to be projected on the reduced basis at each frequency.

In the present work, this is overcome by a decomposition of the system matrix into a frequency-dependent linear combination of frequency-independent global matrices. Although shown to be a computationally viable approach for the isotropic materials studied here, this may become an issue of concern in cases where, for example, the modeling of anisotropic porous materials [24] is required. Alternatively, as done in the present work, these successive frequency-derivative vectors may be used for a component-wise solution expansion via Padé approximants [17–19, 21, 22]. This alternative, within the scope of an FE approach, additionally offers the possibility to directly target the solution reconstruction for a specific DOF subset of interest. While the literature demonstrates the efficiency of this method when applied to single-field problems, it may very well turn out to be advantageous for coupled problems, in particular, when only parts of the solution need to be reconstructed, for example, evaluating the solution only at a restricted number of acoustic DOFs in a complex damped structural-acoustic problem.

In the present approach, such a reconstruction based on Padé approximants is combined with a modal-based reduction of the costly poroelastic domain [10], thus taking advantage of the complementary characteristics of each method: the Padé approximation approach involves an efficient computation of the solution and its derivatives at a very restricted number of frequencies in order to recover the entire frequency response, while a reduced model allows to enhance the computational time both for the solution at these master frequencies and for the reconstruction of the solution in-between [25]. The computational cost of this latter step is in fact linearly related to the number of DOFs involved. Consequently, substantial efficiency improvements could be expected with such a combination, as demonstrated in the present work. In addition, the trade-off between the computational time enhancement and precision loss is discussed in poro-acoustic validation cases.

In the first three sections, the FE formulation, the modal-based reduction of the poroelastic domain, and the Padé approximation method are briefly recalled. More details on the FE formulation and the modal approach can be found in previous works by the authors [10, 25]. An adaptive procedure is then proposed for the decomposition of the frequency range into contiguous frequency intervals of reconstructed response. The last section is dedicated to illustration, validation, and discussion of the approach on poro-acoustic examples.

2. FINITE ELEMENT FORMULATION FOR THE PORO-ACOUSTIC PROBLEM

A poro-acoustic problem is considered, whose description and notations are presented in Figure 1 and Table I. The acoustic fluid and the porous medium occupy the domains Ω_{F} and Ω_{P} respectively.

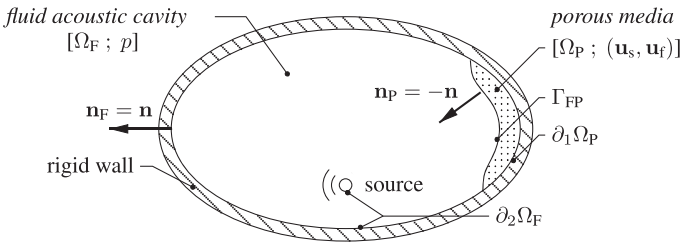

Figure 1. Description and notations of the poro-acoustic interaction problem.

Table I. List of material parameters.

Notation	Description
ρ_s	Density of the material constituting the frame
$(\lambda;\ \mu)$	Lamé parameters for the solid frame
ρ_f	Ambient fluid density
η	Ambient fluid viscosity
P_0	Ambient fluid standard pressure
γ	Heat capacity ratio for the ambient fluid
Pr	Prandtl number for the ambient fluid
ϕ	Porosity
α_∞	Tortuosity
σ	Static flow resistivity
Λ	Viscous characteristic length
Λ'	Thermal characteristic length

The compressible fluid is described using pressure fluctuation (p) as primary variable (Subsection 2.1.1), while the fluid and solid phases homogenized displacements ($\mathbf{u}_s$,$\mathbf{u}_f$) are retained for the porous medium (Section 2.1.2). The domains boundaries are separated into contours of (1) imposed Dirichlet boundary conditions $\partial_1\Omega_F$ and $\partial_1\Omega_P$; (2) prescribed Neumann boundary conditions $\partial_2\Omega_F$ and $\partial_2\Omega_P$; and (3) coupling interface between the acoustic fluid and the porous medium (Γ_{FP}). The FE formulation is presented for a stationary harmonic response at angular frequency ω.

2.1. Dynamic equations and constitutive laws

2.1.1. Compressible fluid (p). The internal fluid within acoustic cavities is assumed to be compressible and inviscid, thus satisfying the Helmholtz equation derived from the motion, continuity, and constitutive equations,

$$\Delta p + \frac{\omega^2}{c_0^2}\, p = 0 \quad \text{in } \Omega_F, \tag{1}$$

where c_0 is the constant speed of sound in the fluid, and p the pressure fluctuation field.

2.1.2. Porous media, Biot theory ($\mathbf{u}_s, \mathbf{u}_f$). At angular frequency ω, the poroelastic medium satisfies the following elastodynamic linearized equations, derived in the Biot–Allard theory [1], taking into account inertia and viscous coupling effects between the solid and fluid phases,

$$\operatorname{div}\boldsymbol{\sigma}_s - \mathrm{i}\,\omega\,\tilde{b}(\omega)(\mathbf{u}_s - \mathbf{u}_f) + \omega^2\left[((1-\phi)\,\rho_s + \rho_a)\,\mathbf{u}_s - \rho_a\mathbf{u}_f\right] = \mathbf{0} \quad \text{in } \Omega_P, \tag{2a}$$

$$\operatorname{div}\boldsymbol{\sigma}_f - \mathrm{i}\,\omega\,\tilde{b}(\omega)(\mathbf{u}_f - \mathbf{u}_s) + \omega^2\left[-\rho_a\mathbf{u}_s + (\phi\rho_f + \rho_a)\mathbf{u}_f\right] = \mathbf{0} \quad \text{in } \Omega_P, \tag{2b}$$

where $\mathbf{u}_s$ and $\mathbf{u}_f$ are the solid phase and fluid phase averaged displacements, respectively, in the sense of the Biot theory. $\tilde{b}(\omega)$ (henceforth denoted as $\tilde{b}$, where $\tilde{(\cdot)}$ refers to a complex-valued quantity) and

ρ_a are the complex frequency-dependent viscous drag and the inertia coupling parameter, respectively, based on the standard notations of these material parameters (see Table I for details of the notations used [1]) and given by

$$\tilde{b} = \sigma\phi^2 \left[1 + \frac{4i\omega\alpha_\infty^2\eta\rho_f}{\sigma^2\Lambda^2\phi^2}\right]^{\frac{1}{2}}, \tag{3}$$

$$\rho_a = \phi\rho_f\,(\alpha_\infty - 1). \tag{4}$$

$\boldsymbol{\sigma}_s$ and $\boldsymbol{\sigma}_f$ are the averaged stress tensors for the solid and fluid phases, respectively. In [10], it was shown that they satisfy the Lagrangian stress-strain relations developed by Biot, rewritten in the following form using Voigt notation,

$$\boldsymbol{\sigma}_s = \mathbf{D}_s^{(1)}\,\boldsymbol{\varepsilon}(\mathbf{u}_s) + \left(\tilde{K}_f - P_0\right)\mathbf{D}_s^{(2)}\,\boldsymbol{\varepsilon}(\mathbf{u}_s) + \mathbf{D}_{sf}^{(1)}\,\boldsymbol{\varepsilon}(\mathbf{u}_f) + \left(\tilde{K}_f - P_0\right)\mathbf{D}_{sf}^{(2)}\,\boldsymbol{\varepsilon}(\mathbf{u}_f), \tag{5a}$$

$$\boldsymbol{\sigma}_f = \mathbf{D}_{sf}^{(1)}\,\boldsymbol{\varepsilon}(\mathbf{u}_s) + \left(\tilde{K}_f - P_0\right)\mathbf{D}_{sf}^{(2)}\,\boldsymbol{\varepsilon}(\mathbf{u}_s) + \mathbf{D}_f^{(1)}\,\boldsymbol{\varepsilon}(\mathbf{u}_f) + \left(\tilde{K}_f - P_0\right)\mathbf{D}_f^{(2)}\,\boldsymbol{\varepsilon}(\mathbf{u}_f), \tag{5b}$$

where $\boldsymbol{\varepsilon}(\mathbf{u}_s)$ and $\boldsymbol{\varepsilon}(\mathbf{u}_f)$ are the strain tensors associated with the averaged displacement fields $\mathbf{u}_s$ and $\mathbf{u}_f$ respectively. $\tilde{K}_f(\omega)$ is the effective bulk modulus of the fluid phase (henceforth denoted by $\tilde{K}_f$),

$$\tilde{K}_f = \frac{\gamma P_0}{\gamma - (\gamma-1)\left[1 + \frac{8\eta}{i\omega Pr\Lambda'^2\rho_f}\left(1 + \frac{i\omega Pr\Lambda'^2\rho_f}{16\eta}\right)^{\frac{1}{2}}\right]^{-1}}. \tag{6}$$

$\mathbf{D}_s^{(1),(2)}$, $\mathbf{D}_f^{(1),(2)}$, and $\mathbf{D}_{sf}^{(1),(2)}$ are constant real-valued constitutive matrices given in [10].

2.2. Fluid-structure interaction problem

2.2.1. Poro-acoustic coupling and boundary conditions. At the external boundary of the acoustic domain, rigid walls are considered, imposing a free pressure field ($\partial_1\Omega_F = \emptyset$).

The time-harmonic source term is given by

$$\mathbf{grad}\; p \cdot \mathbf{n} = \omega^2\rho_F\,u_{Fb} \quad \text{on } \partial_2\Omega_F, \tag{7}$$

where u_{Fb} is non-zero at the acoustic source location only (see $\partial_2\Omega_F$ in Figure 1).

The coupling, at interface Γ_{FP}, is given by the normal stress and normal displacement continuity conditions between the acoustic fluid and both the fluid and solid phases of the porous medium,

$$\boldsymbol{\sigma}_s\,\mathbf{n} + (1-\phi)\;p\,\mathbf{n} = \mathbf{0} \quad \text{on } \Gamma_{FP}, \tag{8a}$$

$$\boldsymbol{\sigma}_f\,\mathbf{n} + \phi\;p\,\mathbf{n} = \mathbf{0} \quad \text{on } \Gamma_{FP}, \tag{8b}$$

$$\mathbf{u}_F \cdot \mathbf{n} - (1-\phi)\mathbf{u}_s \cdot \mathbf{n} - \phi\mathbf{u}_f \cdot \mathbf{n} = 0 \quad \text{on } \Gamma_{FP}, \tag{9}$$

where ϕ is the porosity of the porous material, that is, the volume fraction of fluid.

No external force is applied to the outer boundaries of the porous medium except for the coupling at interface Γ_{FP}. Therefore, $\partial_2\Omega_P = \emptyset$ in the considered problems. Finally, at the external boundary $\partial_1\Omega_P$, two types of boundary conditions can be prescribed, the porous material being considered either as sliding or bonded to a rigid wall (Table II).

2.2.2. Finite element discretized problem. A Galerkin method is used to derive the weak formulation for the coupled problem and the associated discretized set of algebraic equations. Details can be found in [10, 26]. Thus, using the Helmholtz Equation (1), the elastodynamic Equations (2a) and (2b), and the constitutive expressions (5a) and (5b), as well as the acoustic velocity

Table II. Boundary conditions for porous layer on $\partial_1\Omega_\mathrm{P}$.

Bonded layer	Sliding layer
$\mathbf{u}_\mathrm{s} = \mathbf{0}$	$\mathbf{u}_\mathrm{s}\cdot\mathbf{n}_\mathrm{P} = 0$
$\mathbf{u}_\mathrm{f}\cdot\mathbf{n}_\mathrm{P} = 0$	$\mathbf{u}_\mathrm{f}\cdot\mathbf{n}_\mathrm{P} = 0$

source excitation and coupling conditions, the following discretized system of equations may be formulated,

$$\left(\begin{bmatrix} \mathbf{K}_\mathrm{F} & \mathbf{0} & \mathbf{0} \\ -(1-\phi)\mathbf{A}_\mathrm{Fs}^T & \mathbf{K}_\mathrm{ss}^{(1)} & \mathbf{K}_\mathrm{sf}^{(1)} \\ -\phi\mathbf{A}_\mathrm{Ff}^T & \mathbf{K}_\mathrm{sf}^{(1)T} & \mathbf{K}_\mathrm{ff}^{(1)} \end{bmatrix} + \left(\tilde{K}_\mathrm{f} - P_0\right)\begin{bmatrix} \mathbf{0} & \mathbf{0} & \mathbf{0} \\ \mathbf{0} & \mathbf{K}_\mathrm{ss}^{(2)} & \mathbf{K}_\mathrm{sf}^{(2)} \\ \mathbf{0} & \mathbf{K}_\mathrm{sf}^{(2)T} & \mathbf{K}_\mathrm{ff}^{(2)} \end{bmatrix} + \mathrm{i}\,\omega\,\tilde{b}\begin{bmatrix} \mathbf{0} & \mathbf{0} & \mathbf{0} \\ \mathbf{0} & \mathbf{C}_\mathrm{ss} & \mathbf{C}_\mathrm{sf} \\ \mathbf{0} & \mathbf{C}_\mathrm{sf}^T & \mathbf{C}_\mathrm{ff} \end{bmatrix} - \omega^2\begin{bmatrix} \mathbf{M}_\mathrm{F} & (1-\phi)\mathbf{A}_\mathrm{Fs} & \phi\mathbf{A}_\mathrm{Ff} \\ \mathbf{0} & \mathbf{M}_\mathrm{ss} & \mathbf{M}_\mathrm{sf} \\ \mathbf{0} & \mathbf{M}_\mathrm{sf}^T & \mathbf{M}_\mathrm{ff} \end{bmatrix}\right)\begin{bmatrix} \mathbf{P} \\ \mathbf{U}_\mathrm{s} \\ \mathbf{U}_\mathrm{f} \end{bmatrix} = \begin{bmatrix} \omega^2\mathbf{U}_\mathrm{Fb} \\ \mathbf{0} \\ \mathbf{0} \end{bmatrix}. \tag{10}$$

Under the assumption that $\omega \neq 0$, this non-symmetric formulation may be symmetrized in the frequency domain by dividing the acoustic equation by ω^2.

3. MODAL-BASED REDUCTION OF POROELASTIC DOMAIN

As an alternative to the full FE problem (10), the modal-based reduction of the poroelastic domain, as proposed in [10], is used in the present work. The extension of the reduction to the acoustic domain is straightforward and detailed in [26] but not used in this contribution, which is focusing on the poroelastic domain. Thus, non-reduced acoustic DOFs are separated into internal ones (subscript $\bar{I}$) and those at interface with the porous medium (subscript I). Notations used are presented in Figure 2. The solid and fluid phase DOFs (subscripts s and f respectively) are further denoted by a common set of porous DOFs (subscript P), so that the matrix system of Equation (10) may be rewritten as

$$\left[\begin{array}{c|c|c} \mathbf{K}_{\bar{I}\bar{I}} - \omega^2\mathbf{M}_{\bar{I}\bar{I}} & \mathbf{K}_{\bar{I}I} - \omega^2\mathbf{M}_{\bar{I}I} & \mathbf{0} \\ \hline \mathbf{K}_{I\bar{I}} - \omega^2\mathbf{M}_{I\bar{I}} & \mathbf{K}_{II} - \omega^2\mathbf{M}_{II} & -\omega^2\mathbf{A}_{I\mathrm{P}} \\ \hline \mathbf{0} & -\mathbf{A}_{I\mathrm{P}}^T & \begin{array}{c}\mathbf{K}_\mathrm{P}^{(1)} + \left(\tilde{K}_\mathrm{f} - P_0\right)\mathbf{K}_\mathrm{P}^{(2)} + \\ \mathrm{i}\,\omega\,\tilde{b}\,\mathbf{C}_\mathrm{P} - \omega^2\mathbf{M}_\mathrm{P}\end{array} \end{array}\right]\begin{bmatrix} \mathbf{P}_{\bar{I}} \\ \mathbf{P}_I \\ \mathbf{U}_\mathrm{P} \end{bmatrix} = \begin{bmatrix} \omega^2\mathbf{U}_{\bar{I}\mathrm{b}} \\ \mathbf{0} \\ \mathbf{0} \end{bmatrix}, \tag{11}$$

which can be symmetrized by dividing the acoustic equations by ω^2 ($\omega \neq 0$), where $\mathbf{A}_{I\mathrm{P}}$ is the coupling matrix between the interface acoustic DOFs (subscript I) and the porous DOFs (subscript P), given by $\mathbf{A}_{I\mathrm{P}} = [(1-\phi)\mathbf{A}_{I\mathrm{s}} \quad \phi\mathbf{A}_{I\mathrm{f}}]$.

The reduced model is then obtained from a transformation basis including a set of m porous real-valued coupled modes, $\mathbf{\Phi}_{\mathrm{P}m}$, solutions of the eigenvalue problem $\left(\mathbf{K}_\mathrm{P}^{(1)} - \omega^2\mathbf{M}_\mathrm{P}\right)\boldsymbol{\phi} = \mathbf{0}$ and attachment functions, $\mathbf{\Psi}_{\mathrm{P}I} = {\mathbf{K}_\mathrm{P}^{(1)}}^{-1}{\mathbf{A}_{I\mathrm{P}}}^T$, linking the interface acoustic DOFs to the porous DOFs (see [10] for further details). It is given by

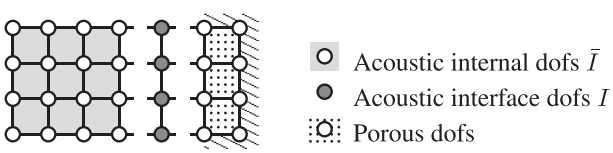

Figure 2. Problem description for modal reduction of porous media.

$$\begin{bmatrix} \hat{\mathbf{P}}_{\bar{I}} \\ \hat{\mathbf{P}}_{I} \\ \hat{\mathbf{U}}_{\mathrm{P}} \end{bmatrix} = \begin{bmatrix} \mathbf{I}_{\bar{I}} & \mathbf{0} & \mathbf{0} \\ \mathbf{0} & \mathbf{I}_{I} & \mathbf{0} \\ \mathbf{0} & \boldsymbol{\Psi}_{\mathrm{P}I} & \boldsymbol{\Phi}_{\mathrm{P}m} \end{bmatrix} \begin{bmatrix} \hat{\mathbf{P}}_{\bar{I}} \\ \hat{\mathbf{P}}_{I} \\ \hat{\boldsymbol{\alpha}}_{m} \end{bmatrix}, \tag{12}$$

where $\hat{(\cdot)}$ denotes an approximation of the original solution, for example, $\begin{bmatrix} \hat{\mathbf{P}}_{\bar{I}} & \hat{\mathbf{P}}_{I} & \hat{\mathbf{U}}_{\mathrm{P}} \end{bmatrix}^T$ is an approximation of $\begin{bmatrix} \mathbf{P}_{\bar{I}} & \mathbf{P}_{I} & \mathbf{U}_{\mathrm{P}} \end{bmatrix}^T$ after modal-based reduction, and $\hat{\boldsymbol{\alpha}}_m$ is the vector of modal coordinates selected after truncation. When applied to a symmetrized form of Equation (11), the transformation leads to the following reduced set of equations,

$$\begin{aligned} \Bigg(& \begin{bmatrix} \frac{1}{\omega^2}\mathbf{K}_{\bar{I}\bar{I}} - \mathbf{M}_{\bar{I}\bar{I}} & \frac{1}{\omega^2}\mathbf{K}_{\bar{I}I} - \mathbf{M}_{\bar{I}I} & \mathbf{0} \\ \frac{1}{\omega^2}\mathbf{K}_{I\bar{I}} - \mathbf{M}_{I\bar{I}} & \frac{1}{\omega^2}\mathbf{K}_{II} - \mathbf{M}_{II} - \mathbf{K}^{(1)}_{\mathrm{P}_{II}} & \mathbf{0} \\ \mathbf{0} & \mathbf{0} & \boldsymbol{\Omega}_m \end{bmatrix} + \left(\widetilde{K}_{\mathrm{f}} - P_0\right) \begin{bmatrix} \mathbf{0} & \mathbf{0} & \mathbf{0} \\ \mathbf{0} & \mathbf{K}^{(2)}_{\mathrm{P}_{II}} & \mathbf{K}^{(2)}_{\mathrm{P}_{Im}} \\ \mathbf{0} & \mathbf{K}^{(2)}_{\mathrm{P}_{mI}} & \boldsymbol{\kappa}_n \end{bmatrix} \\ & + \mathrm{i}\,\omega\,\tilde{b} \begin{bmatrix} \mathbf{0} & \mathbf{0} & \mathbf{0} \\ \mathbf{0} & \mathbf{C}_{\mathrm{P}_{II}} & \mathbf{C}_{\mathrm{P}_{Im}} \\ \mathbf{0} & \mathbf{C}_{\mathrm{P}_{mI}} & \boldsymbol{\zeta}_m \end{bmatrix} - \omega^2 \begin{bmatrix} \mathbf{0} & \mathbf{0} & \mathbf{0} \\ \mathbf{0} & \mathbf{M}_{\mathrm{P}_{II}} & \mathbf{M}_{\mathrm{P}_{Im}} \\ \mathbf{0} & \mathbf{M}_{\mathrm{P}_{mI}} & \mathbf{I}_m \end{bmatrix} \Bigg) \begin{bmatrix} \hat{\mathbf{P}}_{\bar{I}} \\ \hat{\mathbf{P}}_{I} \\ \widehat{\boldsymbol{\alpha}}_m \end{bmatrix} = \begin{bmatrix} \mathbf{U}_{\mathrm{Fb}} \\ \mathbf{0} \\ \mathbf{0} \end{bmatrix}, \end{aligned} \tag{13}$$

where for porous matrices indexed by subscript P, that is, $\mathbf{B}_{\mathrm{P}} \in \{\mathbf{K}^{(1)}_{\mathrm{P}}, \mathbf{K}^{(2)}_{\mathrm{P}}, \mathbf{C}_{\mathrm{P}}, \mathbf{M}_{\mathrm{P}}\}$,

$$\begin{aligned} \mathbf{B}_{\mathrm{P}_{II}} &= \boldsymbol{\Psi}^T_{\mathrm{P}I} \mathbf{B}_{\mathrm{P}} \boldsymbol{\Psi}_{\mathrm{P}I}, \\ \mathbf{B}_{\mathrm{P}_{Im}} &= \boldsymbol{\Psi}^T_{\mathrm{P}I} \mathbf{B}_{\mathrm{P}} \boldsymbol{\Phi}_{\mathrm{P}m} = \mathbf{B}^T_{\mathrm{P}_{mI}}. \end{aligned}$$

The modes included in $\boldsymbol{\Phi}_{\mathrm{P}m}$ are normalized with respect to the porous mass matrix $\mathbf{M}_{\mathrm{P}}$; hence, $\mathbf{I}_m$ is a unit matrix of dimension m, and $\boldsymbol{\Omega}_m$ is a diagonal matrix with, on its diagonal, the m lowest eigenfrequencies resulting from the porous eigenvalue problem, while $\boldsymbol{\kappa}_m$ and $\boldsymbol{\zeta}_m$ are, as detailed in [10], sparsely populated square matrices, defined as $\boldsymbol{\kappa}_m = {\boldsymbol{\Phi}_{\mathrm{P}m}}^T \mathbf{K}^{(2)}_{\mathrm{P}} \boldsymbol{\Phi}_{\mathrm{P}m}$, and $\boldsymbol{\zeta}_m = {\boldsymbol{\Phi}_{\mathrm{P}m}}^T \mathbf{C}_{\mathrm{P}} \boldsymbol{\Phi}_{\mathrm{P}m}$.

In [11], the authors proposed a way to further reduce the size of the modal basis, by sorting and selecting the most contributing components. For the sake of conciseness, the method will not be recalled in the present paper; it is however referred to as the 'reduced optimized' or the 'enhanced reduced' solution in the result section, in contrast with the 'reduced solution', which refers to the modal approach presented in this section.

4. SOLUTION RECONSTRUCTION USING PADÉ APPROXIMANTS

4.1. Presentation and notations

The previously established sets of equations, for the non-reduced problem (symmetrized version of system (10)), for the reduced problem (Equation (13)), and for the further reduced poroelastic problem established in [11], can be expressed in the following frequency-dependent form,

$$\mathbf{Z}(\omega)\mathbf{x}(\omega) = \mathbf{F}(\omega), \tag{14}$$

with $\omega \neq 0$,

$$\mathbf{Z}(\omega) = \frac{1}{\omega^2}\overline{\mathbf{K}}_{\mathrm{F}} + \overline{\mathbf{S}}_{\mathrm{FP}} + \left(\tilde{K}_{\mathrm{f}}(\omega) - P_0\right)\overline{\mathbf{K}}^{(2)}_{\mathrm{P}} + \mathrm{i}\,\omega\,\tilde{b}(\omega)\,\overline{\mathbf{C}}_{\mathrm{P}} - \omega^2\overline{\mathbf{M}}_{\mathrm{P}}, \tag{15}$$

where $\overline{\mathbf{K}}_{\mathrm{F}}$, $\overline{\mathbf{S}}_{\mathrm{FP}}$, $\overline{\mathbf{K}}^{(2)}_{\mathrm{P}}$, $\overline{\mathbf{C}}_{\mathrm{P}}$, and $\overline{\mathbf{M}}_{\mathrm{P}}$ are symmetric, frequency-independent, and real-valued matrices. The notation $\overline{(\cdot)}$ naturally links the terms of Equation (15) to those in Equation (13) or symmetrized Equation (10) given that $\overline{\mathbf{S}}_{\mathrm{FP}}$ accounts for what would be denoted as $\overline{\mathbf{M}}_{\mathrm{F}}$ and $\overline{\mathbf{K}}^{(1)}_{\mathrm{P}}$ and for the fluid-structure coupling terms. In the following, these global assembled matrices refer to either their non-reduced, reduced, or 'enhanced reduced' form. One benefit of the choice made for the poroelastic formulation is manifested in the Padé-based reconstruction scheme, described in the following

section. In fact, having the system matrix frequency-dependence isolated to scalar multiplying functions is a considerable advantage because this simplifies and enhances the application of the Padé approximation compared with a formulation for which derivatives of matrices would have to be considered. For instance, extension of the approach to a displacement-pressure poroelastic formulation, known to be computationally efficient [4], is straightforward but would imply solid and fluid phase-dependent derivatives, thus involving a more complex implementation of the reconstruction scheme.

The proposed Padé procedure, detailed in the following sections, can be decomposed into two main steps: (1) the decomposition of the frequency range of interest into frequency intervals, which will be addressed in Section 5, and (2) for each interval, the resolution of the full problem at a master frequency, followed by the reconstruction of the solution around this point. The latter is presented in the next three sections.

4.2. Determination of the Padé approximants

Given a solution vector $\mathbf{x}(\omega_0)$, the solution around this point, at a given angular frequency ω, can be estimated, for each j-indexed DOF independently, by a rational function of Taylor series expansions. Thus, for each DOF, the solution function (further denoted by $\mathbf{x} \to x_j \to x$ in a simplified notation) can be written as

$$x(\omega_0 + \Delta\omega) \approx \frac{P_L(\Delta\omega)}{Q_M(\Delta\omega)}, \tag{16}$$

with $P_L(\Delta\omega)$ and $Q_M(\Delta\omega)$ being two truncated power series in the variable $\Delta\omega = (\omega - \omega_0)$, to the order L and M respectively, and defined as

$$P_L(\Delta\omega) = \sum_{k=0}^{L} p_k(\Delta\omega)^k, \tag{17a}$$

$$Q_M(\Delta\omega) = \sum_{k=0}^{M} q_k(\Delta\omega)^k. \tag{17b}$$

The approximation of $x(\omega_0+\Delta\omega)$ is then given by the unique determination of the coefficients p_k and q_k. These coefficients can be determined in several ways [27], but a straightforward approach is to consider the Padé approximation as a rearrangement into a rational function of a Taylor series expansion, $A_{L+M}(\Delta\omega)$, to the order $L + M$,

$$\frac{P_L(\Delta\omega)}{Q_M(\Delta\omega)} = A_{L+M}(\Delta\omega) = \sum_{k=0}^{L+M} a_k(\Delta\omega)^k, \tag{18}$$

where

$$a_k = \frac{x^{(k)}(\omega_0)}{k!}, \tag{19}$$

with

$$x^{(0)}(\omega_0) = x(\omega_0) = a_0.$$

Allowing for poles in the rational function ($Q_M(\Delta\omega) = 0$), such an expansion is better suited to account for resonances in the original frequency response than a Taylor series expansion [27–29], which would be very limited in terms of convergence radius. It then follows that the p_k and q_k coefficients are solutions of a system of linear equations established from the constraint

$$P_L(\Delta\omega) - A_{L+M}(\Delta\omega)Q_M(\Delta\omega) = 0, \tag{20}$$

where the coefficients of equal order in $\Delta\omega$ are equated to form a set of $(L+M+1)$ equations. However, this underdetermined system of Equation (20) only gives a solution of the $(L+M+2)$ coefficients within a multiplicative constant. Therefore, these are usually normalized so that the zero-order coefficient of the denominator, q_0, is set to 1 [27], leading to the following set of equations,

$$\left.\begin{aligned} p_0 &= a_0 \\ p_1 - a_0 q_1 &= a_1 \\ &\vdots \\ p_L - a_{L-1}q_1 - \cdots - a_0 q_L &= a_L \\ -a_L q_1 - a_{L-1}q_2 - \cdots - a_{L-M+1}q_M &= a_{L+1} \\ &\vdots \\ -a_{L+M-1}q_1 - a_{L+M-2}q_2 - \cdots - a_L q_M &= a_{L+M} \end{aligned}\right\}, \tag{21}$$

where

$$\begin{cases} a_k = 0 \text{ if } k < 0 \\ q_k = 0 \text{ if } k > M \end{cases}.$$

Subsequently, given the expression of the coefficients a_k in Equation (19), the system of equations arising from the constraint (21) can be written explicitly in a compact form, involving the $(L+M)$ first derivatives of $x(\omega)$ at ω_0,

$$k!\, p_k - \left(\sum_{l=1}^{k} \binom{k}{l} l!\, x^{(k-l)}(\omega_0) q_l \right) = x^{(k)}(\omega_0), \text{ for } k = 0, \ldots, L+M, \tag{22}$$

with

$$\begin{cases} p_k = 0 \text{ if } k > L \\ q_l = 0 \text{ if } l > M \end{cases},$$

and where the binomial coefficients are given by

$$\binom{k}{l} = \frac{k!}{l!(k-l)!}. \tag{23}$$

This set of equations can be solved numerically in a matrix form, for each DOF j, thus involving the resolution of N small problems of dimension $(L+M+1)$,

$$[\mathbf{W}]^{(j)} \begin{bmatrix} p_0 \\ \vdots \\ p_L \\ q_1 \\ \vdots \\ q_M \end{bmatrix}^{(j)} = \begin{bmatrix} x(\omega_0) \\ \vdots \\ x^{(L)}(\omega_0) \\ x^{(L+1)}(\omega_0) \\ \vdots \\ x^{(L+M)}(\omega_0) \end{bmatrix}^{(j)}, \text{ for } j = 1, \ldots, N. \tag{24}$$

For illustration, an example of coefficient matrix $[\mathbf{W}]^{(j)}$ for the approximant ($L = 2, M = 3$), for a given DOF j, at angular frequency ω_0 would then take the form

$$[\mathbf{W}]^{(j)}_{[2,3]} \begin{bmatrix} 0! & 0 & 0 & 0 & 0 & 0 \\ 0 & 1! & 0 & -x^{(0)} & 0 & 0 \\ 0 & 0 & 2! & -2x^{(1)} & -2x^{(0)} & 0 \\ 0 & 0 & 0 & -3x^{(2)} & -6x^{(1)} & -6x^{(0)} \\ 0 & 0 & 0 & -4x^{(3)} & -12x^{(2)} & -24x^{(1)} \\ 0 & 0 & 0 & -5x^{(4)} & -20x^{(3)} & -60x^{(2)} \end{bmatrix}^{(j)} . \tag{25}$$

Note that the system of Equations (24) could be solved in two steps, first solving for the $\{q_1 \cdots q_M\}$ via a system that is equivalent to a Toeplitz system and then retrieving the $\{p_0 \cdots p_L\}$ by simple algebraic operations. Because of this Toeplitz sub-system, the coefficient matrix of system (24) may become rapidly ill-conditioned when increasing the order of the approximants, which in practice, limits the order of expansion that can be achieved in the reconstruction scheme. Furthermore, because of the independent reconstruction of each component of the solution vector, the interval of convergence from one component to the other may vary slightly. In fact, each Padé approximant, corresponding to a component of the reconstructed solution, will in general capture a slightly different subset of the complete system poles. This has, as a consequence, a potential shifting of the bounds for each interval of convergence, handled by an a posteriori error estimator in the present work.

Additionally, in analogy to an approximation of the solution using Taylor series expansion, the solution of the system of Equations (24) requires the determination of the $(L + M)$ derivatives of the solution vector $\mathbf{x}(\omega)$ at ω_0. This aspect is developed further in the following section.

4.3. Successive derivatives of the solution vector

The successive $(L+M)$ derivatives of $\mathbf{x}$ at angular frequency ω_0 can be derived from differentiating Equation (14) with respect to ω. At the order k of differentiation, the following expression arises,

$$\sum_{j=0}^{k} \binom{k}{j} \mathbf{Z}^{(k-j)}(\omega_0)\, \mathbf{x}^{(j)}(\omega_0) = \mathbf{f}^{(k)}(\omega_0), \text{ for } k = 1, \ldots, (L + M), \tag{26}$$

where the zero-order derivatives correspond to the non-differentiated functions. Extracting the highest-order term from the summation in Equation (26) leads to the following recursive expression of $\mathbf{x}^{(k)}(\omega_0)$, that is, the k-order derivative of $\mathbf{x}$ at ω_0,

$$\mathbf{Z}(\omega_0)\, \mathbf{x}^{(k)}(\omega_0) = \mathbf{f}^{(k)}(\omega_0) - \sum_{j=0}^{(k-1)} \binom{k}{j} \mathbf{Z}^{(k-j)}(\omega_0)\, \mathbf{x}^{(j)}(\omega_0), \text{ for } k = 1, \ldots, (L + M). \tag{27}$$

This implies that the successive derivatives of $\mathbf{x}$ with respect to ω, required for the determination of the Padé approximations, can be efficiently computed as the solution of a system of equations of dimension N, with multiple right-hand sides. In fact, the solution can be performed by direct methods using a decomposition of the system matrix. The factorization, as the most time-consuming step of the solution, needs to be carried out once initially, thus providing very efficient multiple solutions of the system. Regarding the multiple right-hand side vectors, they are built from derivatives of the system matrix and lower-order-derivatives of the solution vector. The choices made in this work, particularly regarding the poroelastic formulation where the frequency-dependence is borne by scalar functions, imply inexpensive operations to establish the right-hand side vectors.

4.4. Application to the poro-acoustic problem

4.4.1. Function derivatives. In order to apply the reconstruction procedure, the successive derivatives of $\mathbf{Z}$ (as presented in Equation (15)), with respect to ω, are needed to calculate the right-hand-side vectors in Equation (27). They involve derivatives of four frequency-dependent scalar functions.

Among those, $\tilde{K}_{\mathrm{f}}(\omega)$ and $\omega\,\tilde{b}(\omega)$, being the only non-trivial derivatives, are discussed. The former, introduced in Equation (6), is not expressible in a compact analytic form for its k^{th} derivative. It thus has to be numerically calculated and tabulated and will be referred to as $\tilde{K}_{\mathrm{f}}^{(k)}$ in the following. Regarding $\omega\,\tilde{b}(\omega)$, the viscous drag expression being given in Equation (3), it may be written in the following form,

$$\omega\,\tilde{b}(\omega) = A\omega\,(1+iB\omega)^{\frac{1}{2}}\,, \tag{28}$$

with

$$A = \sigma\phi^2, \tag{29a}$$

$$B = \frac{4\alpha_\infty^2\eta\rho_{\mathrm{f}}}{\sigma^2\Lambda^2\phi^2}. \tag{29b}$$

The derivatives of $\omega\,\tilde{b}(\omega)$ may thus be written as

$$\left(\omega\,\tilde{b}(\omega)\right)^{(1)} = A\,(1+iB\omega)^{\frac{1}{2}} + i\,\frac{AB\omega}{2}\,(1+iB\omega)^{-\frac{1}{2}}\,, \tag{30a}$$

$$\begin{aligned}\left(\omega\,\tilde{b}(\omega)\right)^{(k)} &= (-i)^{k-3}\,\frac{k}{4^{k-2}}\,\frac{|2\,(k-3)+1|!}{|(k-3)|!}AB^{k-1}\,(1+iB\omega)^{-\frac{2(k-2)+1}{2}} \\ &\quad + (-i)^{k-2}\,\omega\,\frac{1}{4^{k-1}}\,\frac{(2\,(k-2)+1)!}{(k-2)!}AB^k\,(1+iB\omega)^{-\frac{2(k-1)+1}{2}} \quad \text{for } k\geqslant 2\end{aligned} \tag{30b}$$

Given $\left(\omega\,\tilde{b}(\omega)\right)^{(k)}$ from Equations (30) and the tabulated expressions of $\tilde{K}_{\mathrm{f}}^{(k)}$, the k^{th} derivative of $\mathbf{Z}$ with respect to ω, for the poro-acoustic problem, is given by

$$\mathbf{Z}(\omega)^{(k)} = \begin{cases} (-1)^k\,(k+1)!\dfrac{1}{\omega^{k+2}}\overline{\mathbf{K}}_{\mathrm{F}} + \tilde{K}_{\mathrm{f}}^{(k)}\overline{\mathbf{K}}_{\mathrm{P}}^{(2)} + \mathrm{i}\,\left(\omega\,\tilde{b}(\omega)\right)^{(k)}\overline{\mathbf{C}}_{\mathrm{P}} - 2\omega\overline{\mathbf{M}}_{\mathrm{P}} & \text{for } k=1 \\ (-1)^k\,(k+1)!\dfrac{1}{\omega^{k+2}}\overline{\mathbf{K}}_{\mathrm{F}} + \tilde{K}_{\mathrm{f}}^{(k)}\overline{\mathbf{K}}_{\mathrm{P}}^{(2)} + \mathrm{i}\,\left(\omega\,\tilde{b}(\omega)\right)^{(k)}\overline{\mathbf{C}}_{\mathrm{P}} - 2\overline{\mathbf{M}}_{\mathrm{P}} & \text{for } k=2 \\ (-1)^k\,(k+1)!\dfrac{1}{\omega^{k+2}}\overline{\mathbf{K}}_{\mathrm{F}} + \tilde{K}_{\mathrm{f}}^{(k)}\overline{\mathbf{K}}_{\mathrm{P}}^{(2)} + \mathrm{i}\,\left(\omega\,\tilde{b}(\omega)\right)^{(k)}\overline{\mathbf{C}}_{\mathrm{P}} & \text{for } k>2 \end{cases} \tag{31}$$

4.4.2. Reconstruction procedure within one frequency interval. Following the derivations presented in the previous sections, the reconstruction of the solution within one frequency interval is done in two main steps:

- Firstly, at a given angular frequency ω_0, the solution and its successive derivatives to the order $(L+M)$ with respect to ω are computed according to Equation (27). This implies, for each angular frequency ω_0 around which the solution is to be approximated, the solution of $(L+M+1)$ problems of dimension N in a multiple right-hand side scheme.
- Then, the solution around ω_0 is reconstructed, for each component of interest, involving the solution of P problems ($P \leqslant N$) of dimension $(L+M+1)$, that is, Equation (24), to determine the Padé approximants corresponding to each DOF. It is then followed by the trivial evaluation of P rational fractions (Equation (16)), for each $\Delta\omega$ at which the approximated solution is to be evaluated.

Given a discretization of the frequency space into intervals associated with their master angular frequency ω_0, the corresponding detailed procedure for one frequency interval is presented in Algorithm 1.

Three points should be further discussed regarding the given description of the proposed procedure. The first one consists in choosing the master frequencies at which the solution will be

Algorithm 1 Steps for solution reconstruction around angular frequency ω_0

1. Compute the system matrix decomposition of Equation (14) at ω_0
2. Solve Equation (14) for the solution $\mathbf{x}(\omega_0)$
3. **for** $j = 1$ **to** $L + M$ **do**
4. Solve Equation (27) for the solution derivative $\mathbf{x}^{(j)}(\omega_0)$
5. **end for**
6. **for** $j = 1$ **to** P **do**
7. Solve Equation (24) for the DOF-dependent Padé approximants
8. Evaluate the approximate multi-frequency solution around ω_0, Equation (16)
9. **end for**

evaluated, that is, setting an appropriate discretization in frequency space. Secondly, for each master frequency, the order of polynomial expansions and the frequency range of evaluation around ω_0 have to be chosen accordingly, which raises the question of the values of L and M. Thirdly, one has to estimate the conditions of efficiency of such an approximation scheme.

Although the second and third points are thoroughly discussed by Avery *et al.* in [18], for single field structural or acoustic applications, the choice of coarse frequencies has, to the knowledge of the authors, not been given much attention in the literature. A suggestion is made in this sense in Section 5 of the present work. Regarding the order of series expansions to consider for both the numerator (L) and the denominator (M), in Equation (16), the following constraint, suggested in [18], reduces the set of possible approximations,

$$M = L + 1. \tag{32}$$

Furthermore, there is an upper limit to the maximum order that can be set, because of the ill-conditioned matrix that arises for the system of Equation (24). Practically, an upper truncation limit is heuristically set for efficiency purposes. It is typically smaller than the numerical limit due to the matrix conditioning issue discussed in the aforementioned text. The truncation is established as a trade-off between the range of convergence achieved by the approximants and the cost associated with the reconstruction steps. In the applications considered in this work, this upper limit is set to $L_{\max} + M_{\max} + 1 = 12$, thus imposing $L_{\max} = 5$, $M_{\max} = 6$. This has proven to be extremely efficient when applied to large single field structural or acoustic applications, with an a priori set frequency discretization of the frequency space [17, 18].

In the following, two extensions to this approach are considered: application of the method to (1) coupled poro-acoustic problems, in which an adaptive frequency discretization scheme is tested, and (2) modal-based reduced versions of these systems of equations, thus estimating the trade-off between the information lost in the reduction itself and the precision needed to establish successive derivatives of the solution. The latter situation would potentially arise in a case where, for example, a reduced-model would be mostly advantageous for memory allocation purposes, while the Padé-based reconstruction could potentially lead to some substantial computational time enhancements.

5. ADAPTIVE DECOMPOSITION IN FREQUENCY INTERVALS

In order to avoid setting an arbitrary, a priori, choice of master frequencies at which the solution is estimated by a direct computation, a straightforward adaptive approach is proposed. It enables a discretization of the frequency space according to the estimated capability of the reconstruction scheme adopted. This limits the lack of precision or the loss in computational efficiency that would be induced by a too coarse or too refined choice for the master frequencies. The idea of an adaptive frequency windowing was first introduced in [14], where it was included in an iterative convergence scheme associated with the Padé-via-Lanczos algorithm. For each frequency step, within one frequency interval of reconstruction, an incremental error comparison between two reduced-order systems of increasing sizes was applied until a convergence criterion was met. Parallel with the

present work, another adaptive scheme was proposed, extended to more general forms of frequency-dependent problems and particularly targeting projection-based interpolatory approaches. In this method as well, residuals were compared between two consecutive steps of increasing size of the reduced system [30]. To implement such incremental approaches would be challenging within the frame of the component-wise interpolatory approach used in the present work, particularly because of computational efficiency considerations. As an alternative, a sequential approach is proposed, combining an a priori estimation of a reasonable master frequency and an a posteriori cost-efficient convergence check and convergence interval refinement. It is based on two aspects: (1) controlling the error of the reconstructed solution using an error estimation performed only at a very restricted number of well-chosen frequencies in the spectrum and (2) using the frequency interval of convergence for each master frequency to anticipate the contiguous frequency interval of convergence.

5.1. Error estimation in the poroelastic domain

For a given approximation of the solution, the error made with respect to the reference FE solution can be estimated from the residue associated with the time-harmonic response. Thus, at a given angular frequency ω, the approximate solution, for example, calculated using a Padé reconstruction procedure, is denoted by $\left[\hat{\hat{\mathbf{P}}}_{\bar{I}} \quad \hat{\hat{\mathbf{P}}}_{I} \quad \hat{\hat{\mathbf{U}}}_{\mathrm{P}}\right]^{T}$, using the same notations as in Equation (11).

From this approximate solution and using the last set of the equations in Equation (11), a residual force vector for the porous domain is computed as

$$\mathbf{R}_{\mathrm{F_P}}(\omega) = \mathbf{A}_{I\mathrm{P}}^{T}\hat{\hat{\mathbf{P}}}_{I} - \left(\mathbf{K}_{\mathrm{P}}^{(1)} + \left(\tilde{K}_{\mathrm{f}}(\omega) - P_0\right)\mathbf{K}_{\mathrm{P}}^{(2)} + \mathrm{i}\,\omega\,\tilde{b}(\omega)\,\mathbf{C}_{\mathrm{P}} - \omega^2\mathbf{M}_{\mathrm{P}}\right)\hat{\hat{\mathbf{U}}}_{\mathrm{P}}. \tag{33}$$

From this, a $\mathbf{K}_{\mathrm{P}}^{(1)}$– residual displacement vector can be established,

$$\mathbf{R}_{\mathrm{U_P}}(\omega) = {\mathbf{K}_{\mathrm{P}}^{(1)}}^{-1}\mathbf{R}_{\mathrm{F_P}}(\omega). \tag{34}$$

This is one of the key aspects, related to efficiency in terms of computational cost, that is at the core of the present method. As $\mathbf{K}_{\mathrm{P}}^{(1)}$ represents the low frequency limit contribution of the coupled stiffness matrix and is independent of frequency, it only needs to be decomposed once, in order to calculate the residual displacement vectors at several selected frequencies through a simple matrix product operation. This residue may then be used to build an error estimator in analogy with the strain energy error estimator used in structural dynamics [31], which may be computed, at selected frequencies, as

$$\varepsilon(\omega) = \frac{\mathbf{R}_{\mathrm{U_P}}^{T}(\omega)\mathbf{K}_{\mathrm{P}}^{(1)}\mathbf{R}_{\mathrm{U_P}}(\omega)}{\hat{\hat{\mathbf{U}}}_{\mathrm{P}}^{\ T}\,\mathbf{K}_{\mathrm{P}}^{(1)}\hat{\hat{\mathbf{U}}}_{\mathrm{P}}} = \frac{\mathbf{R}_{\mathrm{U_P}}^{T}(\omega)\mathbf{R}_{\mathrm{F_P}}(\omega)}{\hat{\hat{\mathbf{U}}}_{\mathrm{P}}^{\ T}\,\mathbf{K}_{\mathrm{P}}^{(1)}\hat{\hat{\mathbf{U}}}_{\mathrm{P}}}. \tag{35}$$

5.2. Adaptive discretization in frequency intervals

It is assumed that the size of the frequency interval of convergence, for a given master frequency, gives a good a priori estimation of the size of its contiguous intervals. This is of course a strong assumption, which might be very case-dependent. However, it is reinforced by the fact that an approximation by a rational function of power series exhibits a rather smooth divergence, particularly when applied to the reconstruction of a smooth function (e.g., a damped response). Consequently, an overestimated interval of convergence implies non-contiguous converged intervals, which may still provide a sensible approximate solution in the gaps. On the contrary, an underestimated interval of convergence implies an overlap of converged intervals, which hinders the computational efficiency by potentially increasing the number of master frequencies needed. Furthermore, it is also assumed that, given an increasing modal density for increasing frequencies, the interval of convergence is expected to decrease with increasing master frequencies. For these reasons, the adaptive reconstruction scheme is started from the higher end of the frequency range

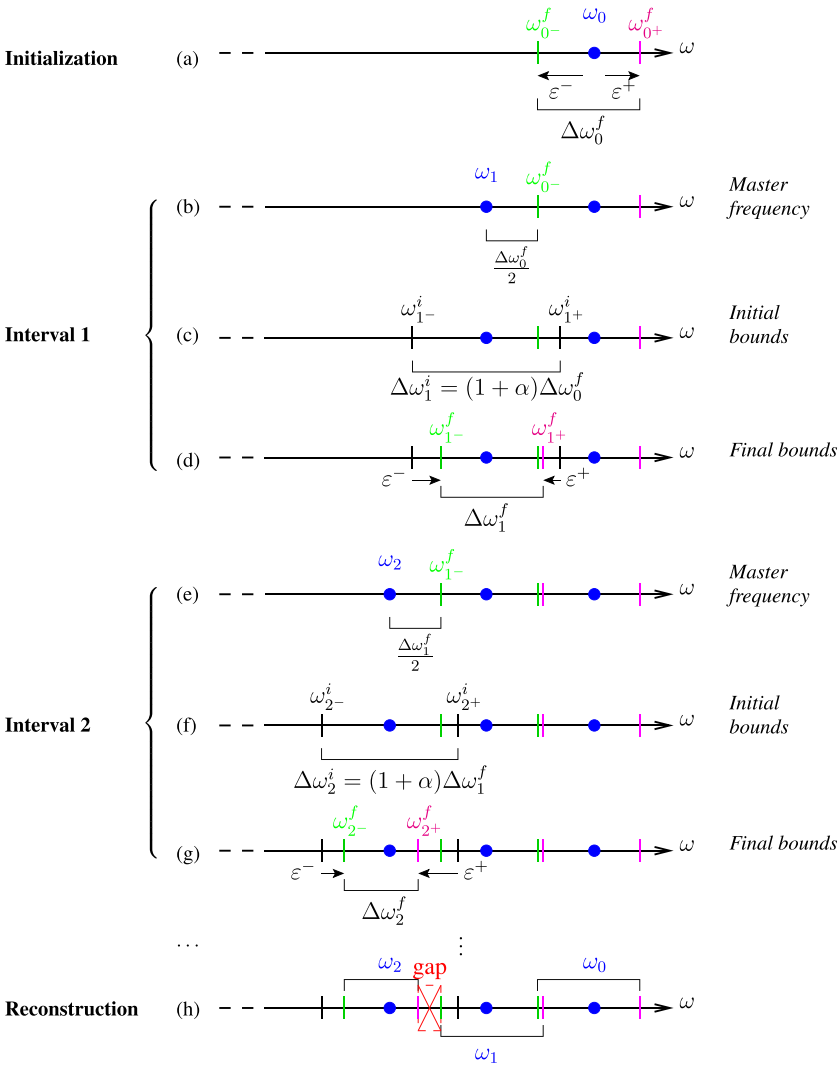

Figure 3. Adaptive frequency interval decomposition: blue, master frequency; magenta, upper limit; and green, lower limit.

and propagated to the lower frequencies with a slight a priori over-estimation of the intervals of convergence. The successive steps are illustrated in Figure 3.

(a) From the first master frequency, corresponding to ω_0, in the higher end of the frequency range, the reconstruction procedure is applied and combined with an error estimation of the approximate solution, that is, $\varepsilon(\omega) \leqslant \varepsilon_{\max}$, where $\varepsilon(\omega)$ is given by Equation (35) and $\varepsilon_{\max}$ is a heuristic tolerance, both towards the lower and the higher frequencies. When the convergence check is no longer satisfied, the corresponding upper and lower limits ω_{0+}^f and ω_{0-}^f define the interval of convergence $\Delta\omega_0^f$, corresponding to the angular frequency ω_0 (the exponent f indicates the final version of these parameters, in contrast to the initial estimations, denoted by exponent i, introduced a priori for upcoming intervals). In the present approach, it is assumed that the upper limit ω_{0+}^f defines the upper bound of the frequency domain of interest.

(b) (resp. (e)) From the previously determined interval of convergence $\Delta\omega_0^f$ (resp. $\Delta\omega_1^f$), the master angular frequency ω_1 (resp. ω_2) associated with the lower-frequency contiguous

interval is estimated. It is positioned 'half-a-convergence-interval' $\frac{\Delta\omega_0^f}{2}$ (resp. $\frac{\Delta\omega_1^f}{2}$) lower than the lower limit ω_{0-}^f (resp. ω_{1-}^f). In doing so, it is anticipated that generally increasing intervals of convergence may result in an overlap of two contiguous converged intervals. However, this choice is made in order to lower the risk of non-converged gaps between intervals (Figure 3(g) and (h)), appearing because of a locally reduced or asymmetric convergence interval.

(c) (resp. (f)) Once the master frequency is established, the upper and lower bounds for the interval, ω_{1+}^i (resp. ω_{2+}^i) and ω_{1-}^i (resp. ω_{2-}^i) respectively, are estimated a priori. They are determined assuming an interval centered on ω_1 (resp. ω_2) and of width $(1+\alpha)\Delta\omega_0^f$ (resp. $(1+\alpha)\Delta\omega_1^f$). The parameter α, which accounts for the anticipation of globally increasing intervals of convergence, is empirically chosen in this work as typically being smaller than 0.2. However, one could argue that α may be a frequency-dependent function in relation with the frequency-dependence of, for example, the modal density, as it is linked to the number of discontinuities per convergence interval. This could be a next step in refining the proposed method.

(d) (resp. (g)) Once a priori estimates of the upper and lower bounds are set, the reconstruction procedure is applied. The error estimation check is simultaneously performed starting from the lower and higher bounds rather than the master frequency. In the numerical tests conducted in the present work, this has been found to reduce the number of points at which the error has to be estimated, thus leading to an improvement of the efficiency of the reconstruction. The actual upper and lower limits of convergence, that is, ω_{1+}^f (resp. ω_{2+}^f) and ω_{1-}^f (resp. ω_{2-}^f) respectively, are determined when the convergence check, based on the error estimation, is satisfied.

While overlapping contiguous convergence intervals have been observed as the foremost outcome (Figure 3(d)), a gap of non-converged reconstructed solution may still arise (Figure 3(g) and (h)) as mentioned in (b).

In case of such gaps in the reconstructed solution, as illustrated in Figure 3(h), two situations may be considered. Firstly, from the error estimations made for frequencies in the gap and from the observed continuity of the solution at the upper bound of the gap, the approximate solution may be deemed acceptable. Otherwise, if a non-acceptable discontinuity in the solution is detected, at the connection between the gap and the upper-frequency converged interval, an increase in the order of truncation of the series or an additional interval may be required. The latter situation, even though probable in case of gross overestimations of convergence intervals, is not considered in the present work where small values of α (typically $\alpha = 0.1$) have been taken into account. Furthermore, following the appearance of such a gap, the converged interval width is presumably reduced compared with the previous established interval. This implies a reset of the overestimation to be made for upcoming intervals and thus introduces another form of adaptivity, inherent to the procedure. Thus, successive gaps in the procedure consequently indicate that α is overestimated.

6. RESULTS AND DISCUSSION

The methods presented are tested on poro-acoustic academic applications. Firstly, the impact of increasing the order of truncation is illustrated on a 1D application, together with a comparison of the precision achieved using Taylor expansions at equivalent orders of truncation. Furthermore, the influence of using Padé approximations on the modal-reduced set of equations is evaluated on the same example. Then, the proposed adaptive reconstruction approach is tested successively on the 2D and 3D versions of the poro-acoustic validation case, both for the complete and reduced set of equations, for which the efficacy of the method is discussed. In order to evaluate the potential of the present approach in a worst case scenario, in terms of efficiency, all components of the solution vectors are reconstructed in the examples presented. Additional gains related to the use of a partial acoustic solution approach for the cavities are thus not accounted for.

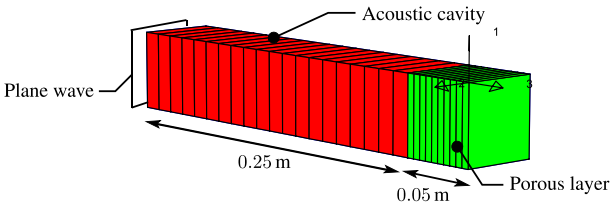

Figure 4. Acoustic cavity mesh and dimensions for 1D problem.

Table III. Air and porous material parameters.

Frame	Fluid	Porous
	$c_0 = 343$ m s^{-1}	$\phi = 0.96$
$\lambda = 905357$ Pa	$\gamma = 1.4$	$\sigma = 32$ kN s m^{-4}
$\mu = 264062$ Pa	$Pr = 0.71$	$\alpha_\infty = 1.7$
$\rho_s = 30$ kg m^{-3}	$\rho_f = 1.21$ kg m^{-3}	$\Lambda = 90\,\mu$m
	$\eta = 1.84 \times 10^{-5}$ N s m^{-2}	$\Lambda' = 165\,\mu$m

6.1. Impact of truncation order, 1D poro-acoustic application

The unidimensional poro-acoustic application is presented in Figure 4, consisting of an acoustic cavity excited with a time-harmonic plane wave, at normal incidence on a poroelastic layer of infinite lateral extent. The rigid cavity is 25 cm long and covered with a 5-cm-thick poroelastic layer at its end. Appropriate Dirichlet boundary conditions are applied to the poroelastic domain to impose unidimensional behavior, thus allowing for solid and fluid displacement in the direction normal to the layer only. In addition, it is considered bonded to a rigid wall at the other surface. Material parameters of the foam are given in Table III. The mesh consists of 20 linear elements for the acoustic domain and 10 linear poroelastic elements in the thickness of the layer, making it a satisfying mesh for the frequency range considered. The 1D FE model thus results in 21 acoustic DOFs and 20 poroelastic DOFs. In order to illustrate the impact of increasing the order of truncation for the power series expansions, the entire frequency range is considered as one interval, whose master frequency is chosen as the middle frequency. The constraint $M = L + 1$ is applied, L varying from 1 to 5. Furthermore, the procedure described in Algorithm 1 is used both for the complete FE model and a model for which the poroelastic domain has been reduced according to the discussion in Section 3. The porous modal basis includes four modes, which proved to be satisfying for the mean quadratic pressure frequency response considered [10]. The results are presented in Figure 5.

Observing the convergence by increasing the order of truncation on the non-reduced set of equations (Figure 5(a)–(e), left figures) illustrates the potential of using Padé approximants for the reconstruction of the solution. In fact, at the 11th order of truncation ($L = 5$, $M = 6$), an interval of almost 1250 Hz of width can be reconstructed from the solution and its derivatives at 1500 Hz. However, besides the fact that the Padé coefficient system to be solved (Equation (24)) becomes rapidly ill-conditioned for orders of truncation above 8–10, the convergence improvements prove to be very significant up to expansions ($L = 3, M = 4$), and slower for higher orders. This can be mostly observed at the upper-bound of the convergence interval for which the frequency response is a rather smooth function of the frequency (range from 2000 to 2250 Hz). To improve the convergence, it is shown in [18] that an approach based on multi-point Padé approximants may become more efficient than an increase in the order of truncation. It is an important aspect of the method to notice that, as already mentioned, the divergence of the approximation immediately out of the convergence interval is relatively slow, particularly for heavily damped systems exhibiting a smooth response.

Considering the reconstruction procedure applied to the reduced set of equations (Figure 5(a)–(e), right figures), it may be noticed that the approximation made in the modal-reduction step does not strongly affect the Padé-based reconstruction. In fact, from the approximant ($L = 4, M = 5$) and onwards, the convergence interval tends to be slightly larger than its non-reduced equivalent

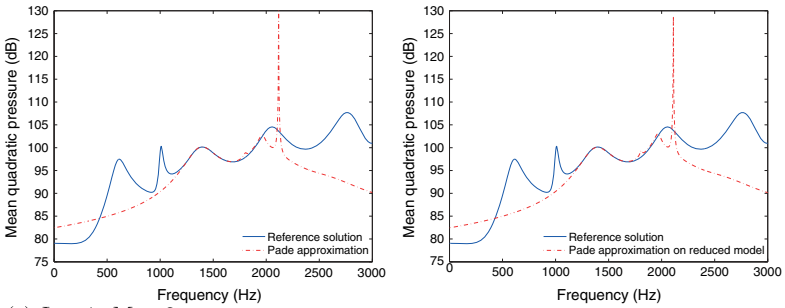

(a) $L = 1$; $M = 2$

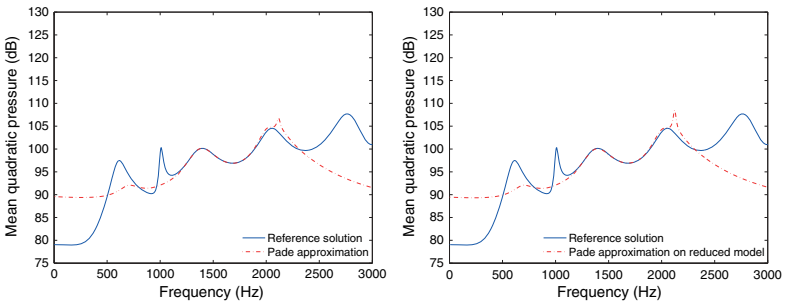

(b) $L = 2$; $M = 3$

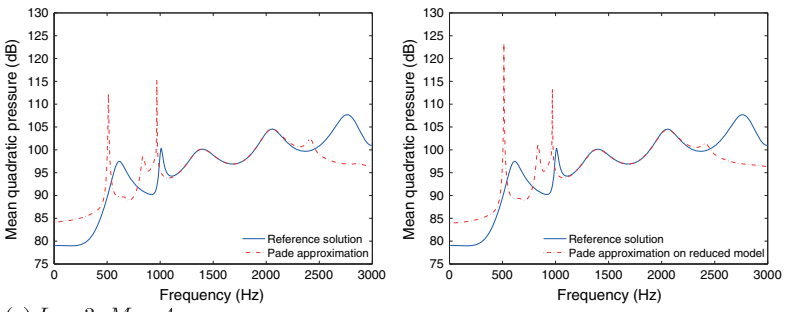

(c) $L = 3$; $M = 4$

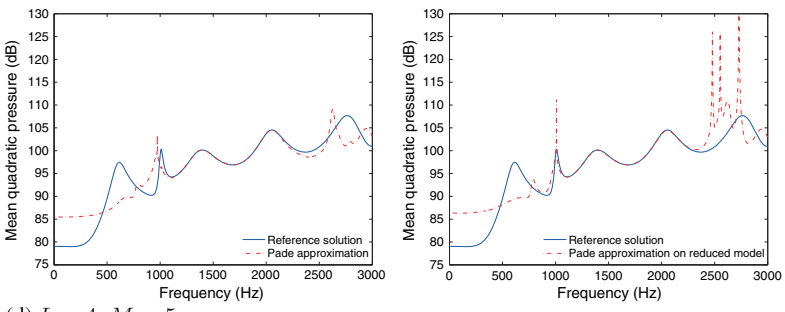

(d) $L = 4$; $M = 5$

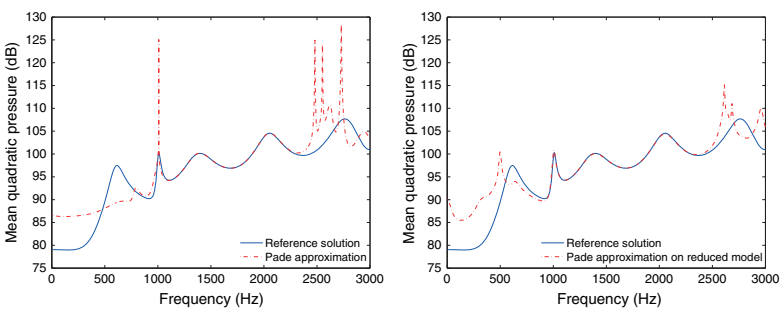

(e) $L = 5$; $M = 6$

Figure 5. Impact of increasing truncation order for power series—1D poro-acoustic problem. Left: Padé on complete problem; Right: Padé on reduced problem.

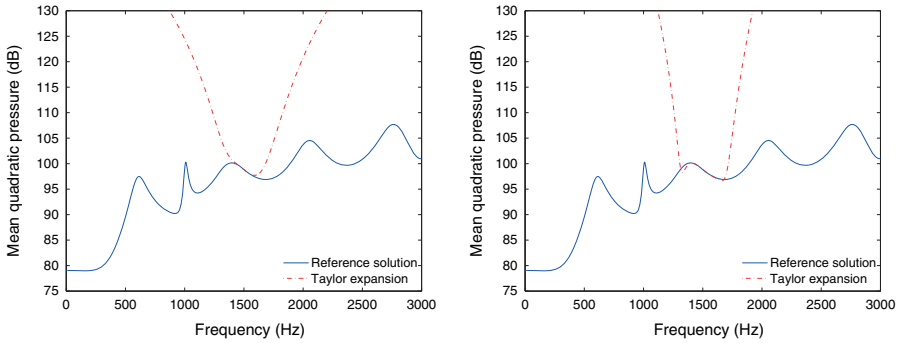

(a) Truncation order 3

(b) Truncation order 5

(c) Truncation order 7

(d) Truncation order 9

Figure 6. Approximation using Taylor expansions—1D poro-acoustic problem.

problem, for example, around the resonance observed at 1000 Hz. This trend has however not been reproduced for more complex problems, such as the 2D or 3D problems considered in the present work. The preserved convergence observed on this application is very promising for efficiency considerations of the method applied to the modeling of porous materials. Thus, for a reduced set of equations, less demanding in terms of memory allocation, the reduction in the number of equation systems (24) to be solved may partly compensate for the extra computational cost involved in establishing the reduced system as such.

Furthermore, the precision achieved using a Padé approach rather than a Taylor series is illustrated in Figure 6 for this 1D application, without modal reduction. Orders of truncation corresponding to those applied with the Padé approach in Figure 5 are used. The comparison demonstrates the expected limitations in terms of interval of convergence using Taylor series, as well as the rapid divergence of the approximation out of this interval.

6.2. Interval decomposition and solution reconstruction on a 2D example

The adaptive procedure presented in Figure 3, to automatically define the master frequencies and the associated interval bounds, is applied to a 2D poro-acoustic problem, whose dimensions and mesh are presented in Figure 7. It consists of an acoustic domain bounded by rigid walls and treated with a porous layer on one wall (material parameters to be found in Table III), having sliding boundary conditions on the side walls and sticking to the back wall. The mesh, including 40×13 linear acoustic elements and 40×12 linear poroelastic elements, is well suited for an analysis up to 2000 Hz [10]. It involves a problem with 574 acoustic DOFs and 1959 poroelastic DOFs. The acoustic domain is excited via a time-harmonic excitation at a corner of the acoustic cavity, opposite to the porous layer.

The initial master frequency is chosen as 1900 Hz. The error estimation limit, imposed in the reconstruction procedure, is empirically set to $\varepsilon_{\max} = 0.1$. In order to assess the influence of lower limits, these have also been tested, with consequences in terms of the response reconstruction as

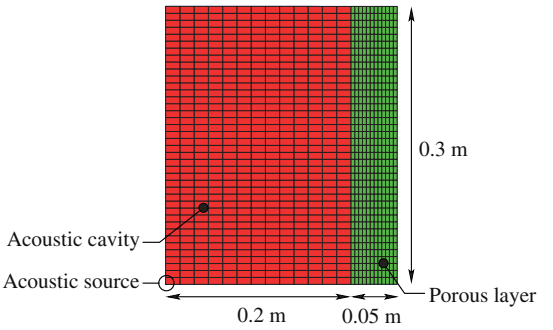

Figure 7. Mesh and dimensions of larger 2D application.

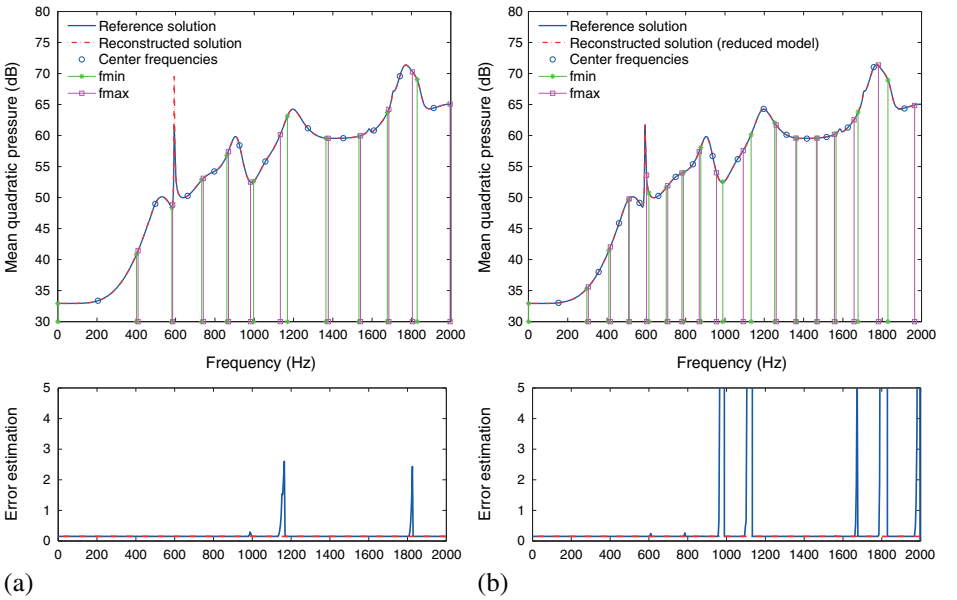

(a) (b)

Figure 8. Adaptive reconstruction procedure applied to 2D problem: (a) from non-reduced problem and (b) from optimized reduced problem.

discussed in the following. On the basis of the observations made in the previous section, the order of truncation is chosen to be an approximant ($L = 3, M = 4$). The results, featuring the reference solution, the reconstructed solution, and the successive intervals represented by their master frequency and their upper and lower bounds, are presented in Figure 8. The solution at the master frequencies, on which the reconstruction procedure is based, is either the one from the complete set of equations (Figure 8(a)) or from the reduced and optimized set of equations (Figure 8(b), see Section 3), established using 88 porous modes in the basis [10, 25]. The reference solution plotted is, in both cases, the one obtained using the complete set of equations. The reconstruction based on the non-reduced reference solution is achieved over 11 frequency intervals (13 and 17 intervals for tolerances of $\varepsilon_{\max} = 0.05$ and $\varepsilon_{\max} = 0.01$ respectively). Even though the approximate solution exhibits an excellent global match with the reference frequency response, except for a non-significant level mismatch at the peak of resonance around 600 Hz, the error estimation underlines three gaps between contiguous intervals (identical for $\varepsilon_{\max} = 0.05$ and $\varepsilon_{\max} = 0.01$). The first one, around 1000 Hz, is hardly noticeable on the error estimation plot itself, while the other two, around 1150 and 1800 Hz, are sufficiently small gaps in smooth ranges of the response to be of minor importance on the reconstructed solution. Applying the Padé-based approximation to the reduced set of poro-acoustic equations (Figure 8(b)) however amplifies those errors. This is rendered by the error estimation plot, where the three previous gaps are found with higher estimated error levels, and

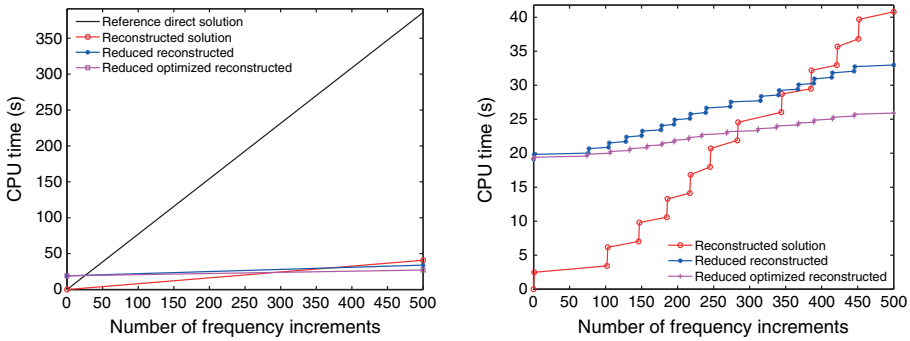

Figure 9. CPU time comparison for the reconstructed solution from the non-reduced, reduced, and optimized reduced 2D problems, approximants ($L = 3, M = 4$): (a) plain and (b) details without reference sweep.

four additional gaps are detected. Among the new gaps, two are minor (around 600 and 800 Hz), one is of little width in a smooth area of the response (around 1700 Hz), and the last one corresponds to the upper range of the frequency range of interest, not matching the upper bound of the initial interval. However, these gaps imply very little mismatch between the reference solution and the reconstructed one, only slightly amplifying the error made by the modal reduction (see, for example, around 1800 Hz). As a consequence to this increase in the estimated error, the adaptive decomposition into frequency intervals exhibits smaller intervals of convergence, thus increasing their number from 11 to 16. Additionally, as being primarily controlled by the overestimation factor α, the gaps observed when lowering the tolerance to $\varepsilon_{\max} = 0.05$ and $\varepsilon_{\max} = 0.01$ appeared to be marginally affected. The same number of gaps were found in the frequency range of interest for this example, some slightly reduced in width. It is further mentioned at this point that the results corresponding to a reduced set of equations, without further downsizing the modal basis, are not presented for the sake of conciseness. They however give the same results as for the reduced and optimized basis, as further detailed in [25]. Thus, the interest in combining the Padé-based reconstruction to a reduced model stands only if the reduced number of times the Padé coefficients equation system (24) has to be solved, restore compensates for the extra operations implied by the increased number of intervals and the construction of the reduced model itself.

A comparison of the CPU times needed for the computation of the direct reference solution, with the Padé-reconstructed solutions based on the following: (1) the complete set of equations; (2) the reduced set of equations; and (3) the optimized-reduced set of equations, is presented in Figures 9 and 10. While Figure 9(a) simply presents the results, Figure 9(b) details the CPU times for the reconstruction of the three reduced problems. The detailed CPU times in Figure 10 are normalized with respect to the reference solution time per increment in order to provide indicative quantifications of the efficiency improvements. Note that, in Figures 9(a) and 10, the CPU time associated with Padé-reconstructed solutions is a frequency-step averaged CPU time, that is, assuming an even distribution of the computational cost over the entire frequency spectrum. In reality, there is a succession of costly steps—full solution and multiple derivatives at a main frequency—and inexpensive steps—expansion of the solution—that are however evenly distributed in the frequency spectrum, as shown in Figure 9(b), thus justifying the approximation of a quasi-step function by a linear interpolation. For the combination of the reduced models with the Padé approach, the comparison is done both with and without accounting for the time to establish the reduced model, the latter being the horizontal asymptote of the former.

Their interpretation provides an answer to the computational efficiency issue raised for the present application. Firstly, for a frequency-sweep with increments of 4 Hz, corresponding to 500 points of computation, the Padé-reconstructed solution based on the complete set of equations is more than 9.5 times as fast as the direct solution, thus confirming the potential of the approach. Arguably, such an efficiency estimation is dependent, among others, on the level of refinement for the frequency

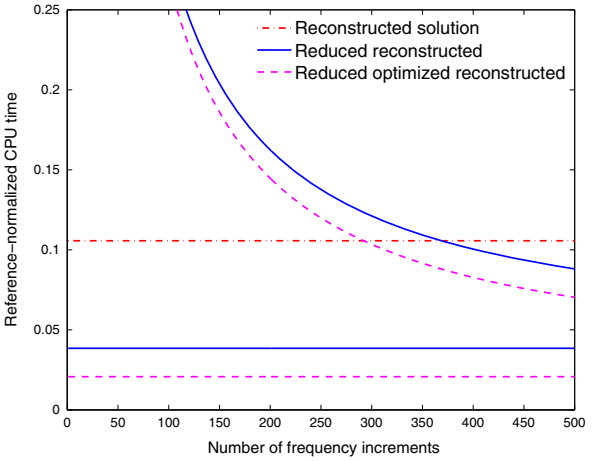

Figure 10. Reference-normalized CPU time comparison for the reconstructed solution of the reduced 2D problems.

sweep (4 Hz increments for this example), which is computationally inexpensive to increase in the case of the Padé-reconstructed solution. Note that, secondly, for the considered application, applying the procedure to the problem with modal-based reduction (optimized or not) of the poroelastic domain is computationally efficient to the extent that it compensates both for the cost of establishing the reduced model—initial step of approximately 20 s for this example—and for the extra intervals needed to accurately rebuild the entire solution. Furthermore, in the best configuration, combining the reduced-optimized model with a Padé reconstruction and disregarding the time allocated to the construction of the reduced model—for example, corresponding to a multiple load case analysis where the reduced model needs to be built for the first case only—the calculation is more than 45 times as fast as for the reference solution. Thus, in addition to saving memory resources, the combination of the Padé-based reconstruction with the modal reduction in the end also has the potential to substantially improve the computational efficiency.

The efficacy analysis, conducted for this 2D poro-acoustic example, points to the following:

- The proposed adaptive decomposition in frequency intervals, for the Padé approximants frequency sweep reconstruction, enables an accurate global solution estimation over the entire frequency range of interest, while limiting the number of complete calculations to be performed.
- The combination of a porous-reduced model with the Padé reconstruction approach allows to maintain a high degree of accuracy, at the cost of a finer discretization of the frequency space.
- The additional computational cost involved by the extra frequency intervals required and the construction of the reduced model is, for the considered 2D example, well compensated by the efficiency improvement of the Padé reconstruction.

These points are further explored and discussed on a 3D application in the next section.

6.3. Adaptive Padé approximation on a 3D poro-acoustic example

In the scope of this work, the combination of a reduced model with the Padé reconstruction strategy is illustrated on a small 3D problem presented in Figure 11. It consists of an acoustic domain filled with air (1872 acoustic DOFs), bounded by rigid walls, and treated with a porous layer on one wall (3070 acoustic DOFs), whose material parameters are given in Table III. Sliding coupling conditions are set for the porous layer along the side walls, and it is assumed to be fixed to the back wall. This example is chosen in order to examine in detail the potential of the algorithm for two different approximants. It is based on a 3D case that is rather conservative in terms of computational performance. The mesh chosen is extremely optimized for the frequency range of interest and does

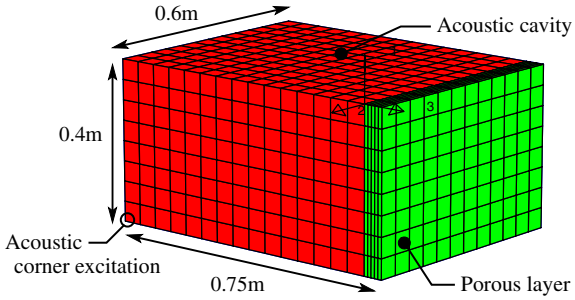

Figure 11. Acoustic cavity mesh and dimensions for 3D problem.

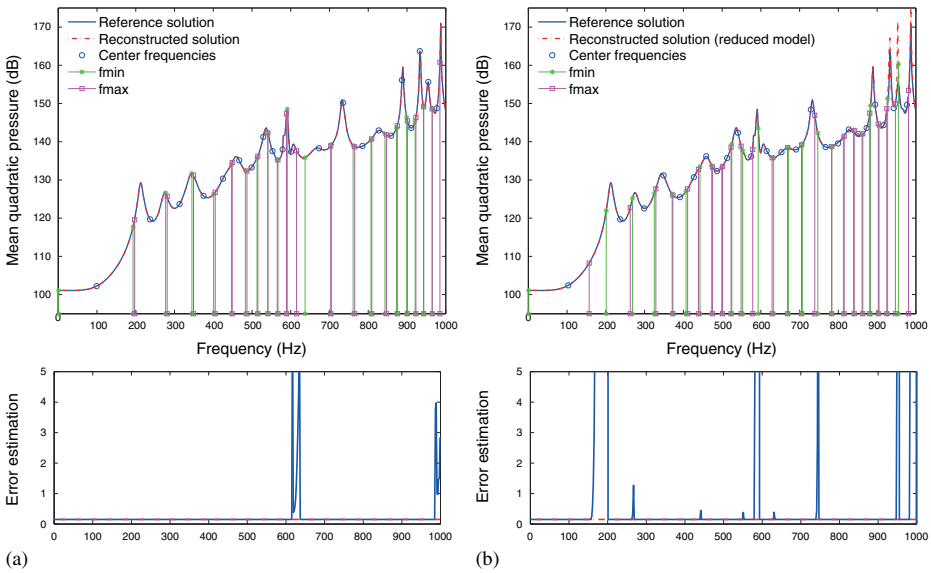

Figure 12. Adaptive reconstruction procedure applied to 3D problem with $L = 3$, $M = 4$: (a) from non-reduced problem and (b) from reduced problem.

not add artificial initial costs to the problem, which would typically be the case for a larger engineering application. Additionally, the same set up was also treated in References [10, 11], where the steps for the modal-based reductions used were discussed, and it allows for a reproduction of the complete numerical procedure leading to the results presented in the following. The example chosen is admittedly academic, but the key findings presented are not biased by the size of the problem as such. The interested reader is referred to Reference [25] for additional examples, particularly if the results on a larger application are sought.

The proposed adaptive reconstruction procedure is presented for the approximants $(L = 3, M = 4)$ and $(L = 5, M = 6)$. In both cases, the initial master frequency is chosen at 1975 Hz. The results are presented for an error estimation limit, $\varepsilon_{\max}$, kept at 0.1. Lower limits of 0.05 and 0.01 have also been checked and commented in the following. These results include the reference solution together with the reconstructed solution and its associated intervals, plotted in Figure 12 for the $(L = 3, M = 4)$ approximant and in Figure 13 for the $(L = 5, M = 6)$ approximant. The Padé-based reconstruction is combined with both the non-reduced FE problem and the porous-reduced models (800 and 83 porous modal coordinates for the reduced and 'enhanced-reduced' models, respectively). The reference solution corresponds to the solution without reduction of the poroelastic domain. The results, without plotting the reconstruction intervals, are given in Figure 14, for the Padé-based reconstruction combined with the enhanced-reduced set of equations. The Padé reconstruction applied to the non-reduced set of equations is achieved over 21 frequency intervals for the $(L = 3, M = 4)$

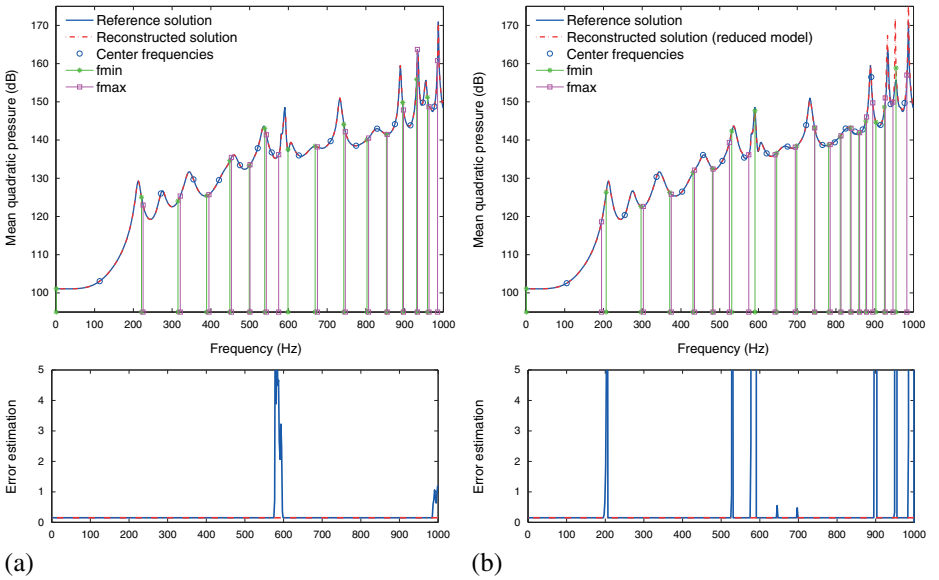

Figure 13. Adaptive reconstruction procedure applied to 3D problem with $L = 5$, $M = 6$: (a) from non-reduced problem and (b) from reduced problem.

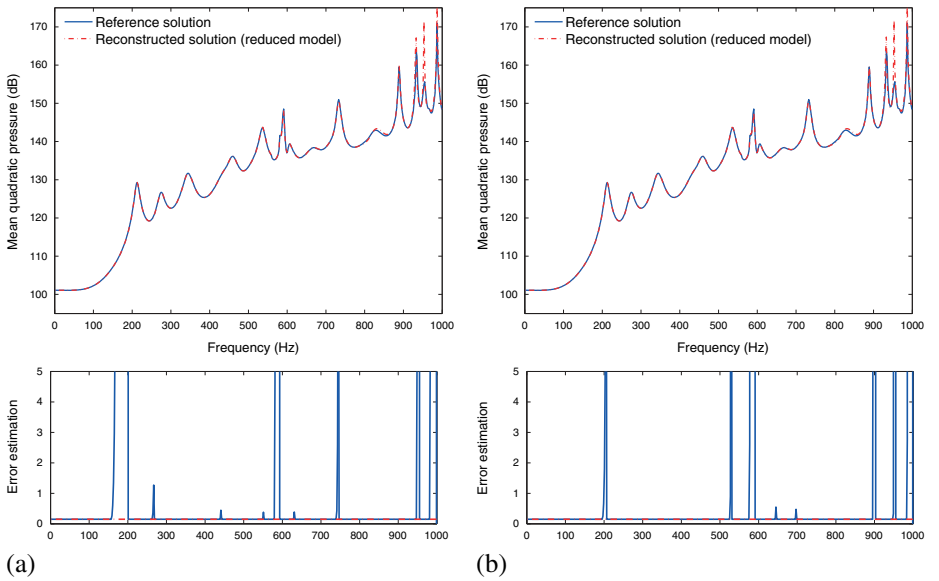

Figure 14. Adaptive reconstructed solution for 3D problem from reduced problem: (a) $L = 3$, $M = 4$ and (b) $L = 5$, $M = 6$.

approximant (Figure 12(a)) and 24 and 26 intervals respectively for $\varepsilon_{\max} = 0.05$ and $\varepsilon_{\max} = 0.01$. It exhibits one gap between approximately 615 and 640 Hz and a solution not converged in upper part of the frequency range of interest, because of the choice of initial master frequency. However, both the choice of limit for the error estimation and the smooth divergence of the method outside of its convergence interval allow for an accurate global reconstruction of the reference solution over the entire frequency range. As shown in Figure 12(b), using a reduced set of equations for the solution at master frequencies implies a loss in precision, resulting in an increase of the estimated error. Thus, the solution is reconstructed over 24 intervals (28 and 30 intervals respectively for $\varepsilon_{\max} = 0.05$ and $\varepsilon_{\max} = 0.01$), to be compared with the 21 intervals previously required (24 and 26 intervals respectively for $\varepsilon_{\max} = 0.05$ and $\varepsilon_{\max} = 0.01$). In addition to the upper bound, eight gaps have

appeared, of which four can be neglected because of both their very narrow frequency intervals and confined estimated errors. Among the four remaining gaps, the one just below 600 Hz is of some concern, considering its location around a resonance frequency, which could justify adding an interval to bridge the gap. However, its width is of approximately 10 Hz, it renders a peak in the frequency response, and its upper bound matches the lower bound of the contiguous interval. These, as confirmed by the comparison with the reference solution, indicate an approximation of the response deemed acceptable. Finally, the gap between 160 and 200 Hz is due to the special treatment applied to the lowest-frequency interval in order to ensure the approximation over the entire frequency range. In fact, in order to both reduce the number of intervals and to ensure the reconstruction until the lowest frequency in the spectrum, the flat response in the very low frequency region is taken to advantage for this example. Thus, when reaching the low frequencies, a larger overestimation factor α is attempted (e.g., $\alpha = 0.5$) and applied only if it allows to reach the lower bound of the frequency spectrum. This explains the larger interval observed at the lowest frequency end, as well as the apparent gap between 160 and 200 Hz. Of little significance in the present analysis, it is not addressed in the presentation of the procedure (Section 5.2) and not further detailed in this work. Again, the matching solution between the upper bound of the gap and the lower bound of the contiguous interval indicates a satisfying approximation. An analogous behavior—and slight decrease in amplitude—of the gaps was observed when lowering the tolerance $\varepsilon_{\max}$ to 0.05 and 0.01.

A similar discussion may be conducted when analyzing the results for the procedure with an approximant ($L = 5, M = 6$), presented in Figure 13. Increasing the order of truncation leads to reconstructed solutions over 15 and 18 intervals for the Padé-based procedure, when applied to the non-reduced and reduced sets of equations, respectively (16 and 20 intervals respectively for $\varepsilon_{\max} = 0.05$ and 17 and 21 intervals respectively for $\varepsilon_{\max} = 0.01$). This is consistent with the larger interval of convergence expected when increasing the order of truncation for the approximants. Again, a very good agreement can be observed between the reference solution and the reconstructed solutions. The only mismatch observed, similar to those of the lower truncation order (Figures 12(b), 13(b), and 14), is the level of the 3 peaks of resonance above 900 Hz. Regarding those, it can be argued that they do not have prime physical significance considering how little damped these resonances are and thus how frequency-shift-dependent their level determination is. Theoretically, they may be explained by the Montessus de Ballore theorem, established in 1902, which stated the uniform convergence of Padé approximants on compact subsets excluding the poles.

The computational efficiency of the approach for this 3D test case is presented in Figures 15 and 16, for the approximant ($L = 5, M = 6$). It includes, in Figure 15(a), a comparison of the estimated computational time for the direct calculation of the reference solution, as well as the Padé-reconstructed solutions based on the following: (1) the complete FE problem; (2) the reduced set of equations (800 porous modal coordinates); and (3) the further reduced set of equations (83

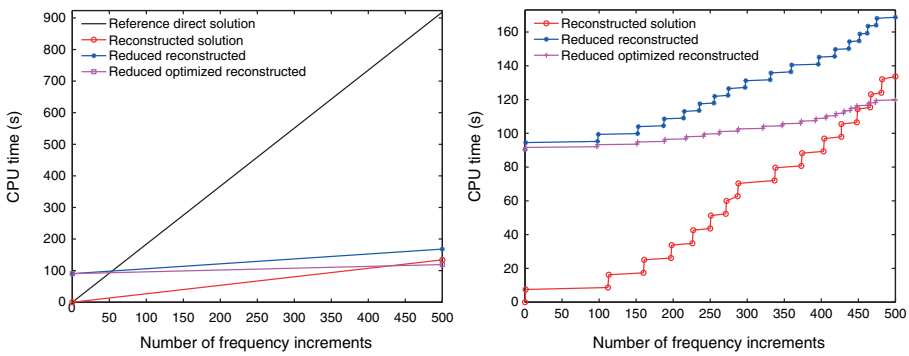

Figure 15. CPU time comparison for Padé-reconstructed solutions of non-reduced, reduced, and optimized reduced 3D problems: (a) plain and (b) details without reference sweep.

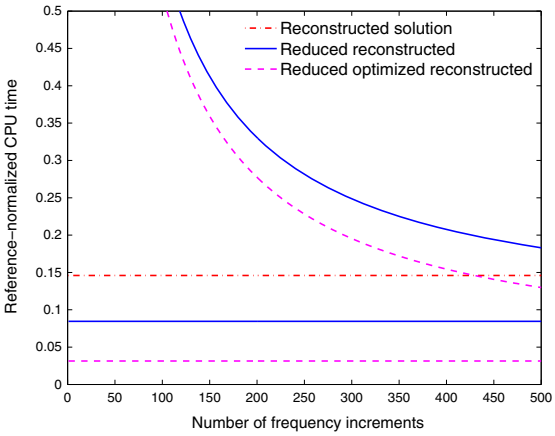

Figure 16. Reference-normalized CPU time comparison for the Padé-reconstructed solutions of the 3D reduced problems.

porous modal coordinates). Figure 15(b) further details these Padé-reconstructed reduced solutions, and Figure 16 presents their reference-normalized CPU times.

Thus, using a Padé-based reconstruction approach leads to a frequency sweep more than 6.5 times as fast as for a direct approach, considering frequency increments of 2 Hz for this 3D application. Combining it to a modal-based reduced set of equations does not substantially reduce the overall computational time, if accounting for the time allocated to establish the reduced problem. However, the averaged time per frequency increment is greatly improved, even compensating for the cost of building the reduced model if the optimized modal basis is used. In a multiple response analysis, the combination of the Padé reconstruction with the optimized reduced problem thus enables a speed-up factor of almost 35. Though not presented in this paper (see [25] for further details), there is very little computational time improvement between the use of approximant ($L = 3$, $M = 4$) and approximant ($L = 5$, $M = 6$), thus confirming that there is a trade-off to be found. In fact, there is a limit above which, increasing the order of truncation does not substantially increase the intervals width of convergence. This implies little reduction in the number of master frequencies at which the complete solution has to be calculated, thus not compensating for the increased size of the Padé coefficient system to be solved (Equation (24)) for each DOF. For the applications considered in the scope of this work, the order of truncation ($L = 3$, $M = 4$) has shown to be a good compromise for computational efficiency, while ensuring a well-conditioned Padé coefficient system matrix. While the academic examples considered offer the possibility to detail the efficacy analysis, additional validation cases have been performed by the authors, available in [25], on larger problems, confirming the demonstrated performance of the approach.

7. CONCLUSION

In this contribution, a Padé-based reconstruction method was extended to a modal reduction of poroelastic domains in poro-acoustic problems. Such a combined approach takes advantage of the complementary properties of these methods. Firstly, using a modal-based reduced problem saves memory resources and offers substantial computational improvements, particularly if a multiple load solution is sought. The reconstruction approach then substantially enhances the resolution efficiency over the frequency range of interest, by reducing the set of frequencies at which the solution has to be calculated. While being strongly application-dependent, improvements by an order of magnitude were observed on the conservative validation cases considered, in terms of computational cost. The observed loss in precision, due to the reduction, implies the need for a finer decomposition in frequency intervals for the reconstruction scheme. However, this increase in the number of master frequencies is shown to be more than compensated by the improved efficiency of the reconstruction,

due to the reduced number of DOFs. For the considered example, it even compensates for the initial computational cost allocated to establish the reduced model. Particularly, in situations where multiple frequency response estimations are required, for example, for topology optimization or multiple load cases analysis, the reduced model needs to be established once for the first solution only, thus allowing speed-up factors up to around 50 for the subsequent solutions, as shown for the presented test cases.

Furthermore, an adaptive approach was proposed in order to automatically determine the master frequencies at which the complete direct solutions have to be computed and around which the solution is approximated. It involves using an error estimation associated with the solution around each master frequency, thus establishing frequency intervals of the converged solution. Each interval is then used to estimate, a priori, the frequency interval of convergence for the neighboring master frequency, before some a posteriori adjustments. This straightforward approach proved to produce accurate frequency responses in a very computationally efficient way, for the configurations tested. Thus, a priori knowledge of the dynamic behavior is not required for the choice of master frequencies. In the end, this reduces the risk of setting a too coarse or too fine a priori discretization in frequency intervals, which would either hamper the solution accuracy or efficiency.

ACKNOWLEDGEMENTS

The research presented in this paper was partly state-funded by a doctoral grant of the French Ministry of Higher Education and Research and partly performed as part of the Marie Curie RTN and ITN projects: 'A Computer Aided Engineering Approach for Smart Structures Design' (MC-RTN-2006-035559) and 'MID-FREQUENCY – CAE Methodologies for Mid-Frequency Analysis in Vibration and Acoustics' (GA-214909). The authors also gratefully acknowledge the financial and scientific support of the Centre for ECO^2 Vehicle Design.

REFERENCES

1. Allard JF, Atalla N. *Propagation of Sound in Porous Media: Modelling Sound Absorbing Materials*. Wiley: New York, 2009.
2. Bermúdez A, Rodríguez R. Modelling and numerical solution of elastoacoustic vibrations with interface damping. *International Journal for Numerical Methods in Engineering* 1999; **46**(10):1763–1779. DOI: 10.1002/(SICI)1097-0207(19991210)46:10.1763::AID-NME723.3.0.CO;2-6.
3. Deü JF, Larbi W, Ohayon R. Vibration and transient response of structural-acoustic interior coupled systems with dissipative interface. *Computer Methods in Applied Mechanics and Engineering* 2008; **197**(51-52):4894–4905.
4. Atalla N, Hamdi MA, Panneton R. Enhanced weak integral formulation for the mixed (u,p) poroelastic equations. *The Journal of the Acoustical Society of America* 2001; **109**(6):3065–3068. DOI: 10.1121/1.1365423.
5. Kang YJ, Bolton JS. Finite element modeling of isotropic elastic porous materials coupled with acoustical finite elements. *The Journal of the Acoustical Society of America* 1995; **98**:635–643.
6. Panneton R, Atalla N. An efficient finite element scheme for solving the three-dimensional poroelasticity problem in acoustics. *The Journal of the Acoustical Society of America* 1997; **101**(6):3287–3298. DOI: 10.1121/1.418345.
7. Hörlin NE, Nordström M, Göransson P. A 3-D hierarchical FE formulation of Biot's equations for elasto-acoustic modelling of porous media. *Journal of Sound and Vibration* 2001; **245**(4):633–652.
8. Davidsson P, Sandberg G. A reduction method for structure-acoustic and poroelastic-acoustic problems using interface-dependent Lanczos vectors. *Computer Methods in Applied Mechanics and Engineering* 2006; **195**(17-18):1933–1945.
9. Dazel O, Brouard B, Dauchez N, Geslain A, Lamarque CH. A free interface CMS technique to the resolution of coupled problem involving porous materials, application to a monodimensional problem. *Acta Acustica united with Acustica* 2010; **96**(2):247–257.
10. Rumpler R, Deü JF, Göransson P. A modal-based reduction method for sound absorbing porous materials in poro-acoustic finite element models. *The Journal of the Acoustical Society of America* 2012; **132**(5):3162–3179.
11. Rumpler R, Göransson P, Deü JF. A residue-based mode selection and sorting procedure for efficient poroelastic modeling in acoustic finite element applications. *The Journal of the Acoustical Society of America* 2013; **134**(6):4730–4741. DOI: 10.1121/1.4824966.
12. Feldmann P, Freund R W. Efficient linear circuit analysis by Padé approximation via the Lanczos process. *IEEE Transactions on Computer-Aided Design of Integrated Circuits and Systems* 1995; **14**(5):639–649. DOI: 10.1109/43.384428.
13. Wagner MM, Pinsky PM, Malhotra M. Application of Padé via Lanczos approximations for efficient multifrequency solution of Helmholtz problems. *The Journal of the Acoustical Society of America* 2003; **113**(1):313–319. DOI: 10.1121/1.1514932.

14. Tuck-Lee JP, Pinsky PM. Adaptive frequency windowing for multifrequency solutions in structural acoustics based on the matrix Padé-via-Lanczos algorithm. *International Journal for Numerical Methods in Engineering* 2008; **73**(5):728–746. DOI: 10.1002/nme.2102.
15. Liew HL, Pinsky PM. Matrix-Padé via Lanczos solutions for vibrations of fluid-structure interaction. *International Journal for Numerical Methods in Engineering* 2010; **84**(10):1183–1204. DOI: 10.1002/nme.2936.
16. Bai Z, Su Y. Dimension reduction of large-scale second-order dynamical systems via a second-order Arnoldi method. *SIAM Journal on Scientific Computing* 2005; **26**(5):1692–1709.
17. Djellouli R, Farhat C, Tezaur R. A fast method for solving acoustic scattering problems in frequency bands. *Journal of Computational Physics* 2001; **168**(2):412–432.
18. Avery P, Farhat C, Reese G. Fast frequency sweep computations using a multi-point Padé-based reconstruction method and an efficient iterative solver. *International Journal for Numerical Methods in Engineering* 2007; **69**(13):2848–2875. DOI: 10.1002/nme.1879.
19. Jensen JS. Topology optimization of dynamics problems with Padé approximants. *International Journal for Numerical Methods in Engineering* 2007; **72**(13):1605–1630.
20. Beattie C, Gugercin S. Interpolatory projection methods for structure-preserving model reduction. *Systems & Control Letters* 2009; **58**(3):225–232. DOI: 10.1016/j.sysconle.2008.10.016.
21. Chazot JD, Nennig B, Chettah A. Harmonic response computation of viscoelastic multilayered structures using a ZPST shell element. *Computers & Structures* 2011; **89**(23-24):2522–2530.
22. Hetmaniuk U, Tezaur R, Farhat C. Review and assessment of interpolatory model order reduction methods for frequency response structural dynamics and acoustics problems. *International Journal for Numerical Methods in Engineering* 2012; **90**(13):1636–1662.
23. Souza Lenzi M, Lefteriu S, Beriot H, Desmet W. A fast frequency sweep approach using Padé approximations for solving Helmholtz finite element models. *Journal of Sound and Vibration* 2013; **332**(8):1897–1917. DOI: 10.1016/j.jsv.2012.05.038.
24. Hörlin NE, Göransson P. Weak, anisotropic symmetric formulations of Biot's equations for vibro-acoustic modelling of porous elastic materials. *International Journal for Numerical Methods in Engineering* 2010; **84**(12):1519–1540. DOI: 10.1002/nme.2955.
25. Rumpler R. Efficient finite element approach for structural-acoustic applicationns including 3D modelling of sound absorbing porous materials. *Ph.D. Thesis*, Cnam/KTH, 2012.
26. Rumpler R, Legay A, Deü JF. Performance of a restrained-interface substructuring FE model for reduction of structural-acoustic problems with poroelastic damping. *Computers & Structures* 2011; **89**(23-24):2233–2248.
27. Baker GA, Graves-Morris PR. *Padé Approximants*, Vol. 59. Cambridge University Press: Cambridge, 1996.
28. Bender C, Orszag S. *Advanced Mathematical Methods for Scientists and Engineers: Asymptotic Methods and Perturbation Theory*, Vol. 1. Springer Verlag: New York, 1999.
29. Cochelin B, Damil N, Potier-Ferry M. *Méthode Asymptotique Numérique*. Hermès - Lavoisier: Paris, 2007.
30. Hetmaniuk U, Tezaur R, Farhat C. An adaptive scheme for a class of interpolatory model reduction methods for frequency response problems. *International Journal for Numerical Methods in Engineering* 2013; **93**(10):1109–1124. DOI: 10.1002/nme.4436.
31. Kergourlay G, Balmès E, Clouteau D. Model reduction for efficient FEM/BEM coupling. *Proceedings of the international seminar on modal analysis*, Kissimee Florida, 2001; 1167–1174.